# Super-Resolution Joint Azimuth-Range-Doppler Estimation via OFDM Waveforms



Citation for the original published paper (version of record):
Li, X., Yi, W., Cao, Z. et al (2026). Super-Resolution Joint Azimuth-Range-Doppler Estimation via OFDM Waveforms. IEEE Transactions on Aerospace and Electronic Systems, 62: 10958-10976.
http://dx.doi.org/10.1109/TAES.2026.3692467

# Super-Resolution Joint Azimuth-Range-Doppler Estimation via OFDM Waveforms

Xile Li, *Student Member, IEEE*, Wei Yi, *Senior Member, IEEE*, Ziyi Cao, Alireza Pourafzal, *Member, IEEE*, and Henk Wymeersch, *Fellow, IEEE*

***Abstract*—This paper considers the problem of super-resolution estimation of multi-dimensional target parameters using orthogonal frequency division multiplexing (OFDM) waveforms. Existing super-resolution techniques primarily focus on either angle estimation or range-Doppler estimation. Attempting to obtain high-dimensional parameter estimates by separately estimating angle, range, and Doppler and then pairing the results often leads to parameter mismatches and target identification ambiguity. To address this issue, we propose an extended propagator method that employs a 3D affine subarray mapping to fully exploit inter-source phase variations and avoid rank deficiency in multidimensional problems. By vectorizing the received data and applying forward-backward smoothing, the cross-dimensional estimation problem is reformulated as a multivariate phase-rotation estimation problem. The final parameters are obtained via an orthogonal-propagator-based spatial spectrum search, achieving accurate high-resolution estimation without covariance matrix construction or eigenvalue computation. To further reduce computational complexity, a dimension-reduced sequential estimation framework is introduced. Under the considered simulation settings (e.g., standard 5G configurations with limited data size and moderate-to-high SNR), the proposed approach reduces computational complexity by approximately two to three orders of magnitude, at the cost of only about a 10% increase in RMSE. The proposed method is theoretically formulated in a general form, and a two-stage implementation is illustrated using Doppler estimation following range-angle estimation. Both simulations and experiments based on a 5G-band OFDM ISAC platform validate the effectiveness of the proposed approach.**

***Index Terms*—Orthogonal frequency division multiplexing (OFDM), joint azimuth-range-Doppler estimation, super-resolution, radar and sensing, integrated sensing and communication (ISAC).**

## I. INTRODUCTION

ORthogonal Frequency Division Multiplexing (OFDM) is a multicarrier modulation technique composed of multiple orthogonal subcarriers. It offers advantages such as robustness against multipath fading [1], high spectral efficiency, and ease of implementation [2]. Owing to these characteristics, OFDM has been widely adopted in 4G and 5G communication systems and is considered a key waveform for future 6G networks [3]. With the rapid proliferation of wireless devices and increasing scarcity of spectrum resources, bandwidth congestion has become a critical issue, driving the development of integrated sensing and communication (ISAC) technologies [4]. Meanwhile, future wireless sensing devices, such as radars, are expected to support communication functionalities [5]. As a result, considerable research efforts have been dedicated to enhancing the sensing capabilities of OFDM waveforms [6], [7]. Representative applications include LTE-based sensing networks [8], 5G hardware platforms [9], and intelligent transportation systems [10].

Target parameter estimation is a fundamental and critical task in OFDM-based sensing systems. Accurate acquisition of these parameters reflects the spatial and motion characteristics of targets and provides essential information for subsequent functions such as detection, localization, and tracking. In sensing applications, key parameters to be estimated typically include the target's azimuth angle, range, and velocity. Conventionally, these parameters are estimated sequentially. Specifically, digital beamforming (DBF) [11] or discrete Fourier transform (DFT) [12] is first employed to focus energy in the angular domain for angle estimation. Subsequently, range and Doppler parameters of illuminated targets are estimated along the beam direction using techniques such as periodogram-based methods [13], [14] and matched filtering (MF) [15]. However, the resolution of these methods is fundamentally constrained by the array aperture and signal bandwidth, making further improvement costly in terms of hardware and spectrum resources.

In recent years, high-resolution estimation techniques have been introduced into OFDM-based parameter estimation to surpass the resolution limits imposed by classical Fourier-transform-based methods [16]–[23]. These methods extract spatial features directly from raw echoes or covariance data, allowing precise separation of closely spaced targets. One main focus is high-resolution azimuth estimation, which is essential in OFDM sensing and closely tied to the role of beamforming in wireless communications [16]. Among various approaches, subspace-based algorithms [17], [24] are the most commonly adopted. These methods exploit the multicarrier nature of OFDM to effectively increase the number of snapshots associated with steering vectors in the angular domain, thereby enhancing angular estimation performance. Maximum likelihood (ML) estimation techniques [16] have also been shown to achieve comparable accuracy. Furthermore, when targets and clutter exhibit sparsity, compressed sensing

Xile Li, Wei Yi, and Ziyi Cao are with the School of Information and Communication Engineering, University of Electronic Science and Technology of China, Chengdu 611731, China (e-mail: luestcer@gmail.com; kussoyi@gmail.com; hellocaoziyi@gmail.com).

Alireza Pourafzal and Henk Wymeersch are with the Department of Electrical Engineering, Chalmers University of Technology, 412 96 Gothenburg, Sweden (e-mail: alireza.pourafzal@chalmers.se; henkw@chalmers.se).

This work was supported in part by the National Natural Science Foundation of China under Grant No. 62231008, in part by the Natural Science Foundation of Sichuan Province under Grant No. 2026NSFSCZY0130, in part by the Swedish Research Council under Grant No. 2022-03007, and in part by the Vinnova B5GPOS Project under Grant No. 2022-01640.

(CS)-based methods [18] can directly extract target parameters from the received signals. In addition, OFDM-based super-resolution algorithms for range-Doppler estimation have also been extensively studied. Researchers have proposed leveraging the subcarrier and symbol dimension to construct multi-channel inputs corresponding to two-dimensional steering vectors. Representative algorithms include the multiple signal classification (MUSIC) method [19] and the estimation of signal parameters via rotational invariance techniques (ESPRIT) [21]. Both ML and CS techniques have also been extended to this domain [22], [23].

The aforementioned methods effectively achieve high-resolution estimation of single or dual parameters. However, directly combining them to jointly estimate multiple parameters such as angle, range, and Doppler is generally challenging. In particular, estimating parameters separately along different dimensions and subsequently matching them to form multidimensional estimates often leads to target identification ambiguities. This is especially problematic in multi-target scenarios, where distinguishing true parameter combinations from false ones becomes challenging.

To address this issue, a promising approach is to develop joint super-resolution algorithms that directly exploit the structured 3D data cube formed by OFDM signals, particularly subspace-based methods [25], [26].These methods remain directly applicable after vectorizing the multidimensional steering vector into a Kronecker form, which preserves the array degrees of freedom and allows a large number of sources to be resolved, without relying on additional structural assumptions such as sparsity [27] or uniqueness in tensor decompositions [28]. In our earlier work, we proposed a joint estimation approach based on the MUSIC algorithm [25]. More recently, a three-dimensional (3D) joint ESPRIT algorithm using OFDM waveform was introduced in [26]. Despite these advances, subspace methods often suffer from high computational cost due to large covariance construction and eigen-decomposition. Moreover, rotational-invariance-based methods, such as ESPRIT and its variants, may exhibit increased sensitivity to modeling errors compared with spectrum-based techniques [29].

In this paper, we focus on joint azimuth-range-Doppler super-resolution estimation within a monostatic OFDM system. The main contributions are summarized as follows:

1) *An efficient super-resolution joint azimuth-range-Doppler estimator with OFDM waveform*: To avoid the heavy cost of covariance construction and eigen-decomposition on high-dimensional data, we propose a new method based on the propagator method [30]. Unlike previous techniques, a 3D affine subarray mapping is employed to fully exploit inter-source phase variations across all dimensions. This mapping preserves the multidimensional phase structure, ensures uniqueness in the linear representation, and prevents the subarray rank deficiency that may arise when directly applying the propagator method to multidimensional problems. As a result, accurate subspace extraction and high-resolution estimation can be achieved. The received data are vectorized to reformulate cross-dimensional estimation as multivariate phase rotation, with forward-backward smoothing applied to mitigate snapshot correlation. Finally, parameters are obtained through a spatial spectrum search generated by the orthogonal propagator, yielding improved robustness under the considered simulation setup relative to the baseline 3D ESPRIT implementation.
2) *A low-complexity sequential multi-parameter estimation framework*: To further reduce the burden of high-dimensional spectrum search, we propose a sequential framework that estimates parameters in stages. Parameters corresponding to partial dimensions are first obtained via matrix unfolding, after which the projection matrix is reduced and the remaining parameters are jointly estimated with automatic matching. This sequential framework lowers both the steering vector dimension and search space, enabling high-resolution estimation with much lower complexity. A two-stage azimuth-range-before-Doppler model is provided as an implementation example.
3) *Verification via simulations and practical 5G band OFDM-based ISAC devices*: We perform numerical simulations to evaluate the complexity and accuracy trade-offs of both methods. Additionally, we validate the proposed algorithms using a practical 5G-band OFDM-based ISAC experimental system tested with unmanned aerial vehicles (UAVs).

The rest of this paper is organized in the following manner. The OFDM sensing system model, including the transmit, measurement, and reconstructed signal models, as well as the problem statement, is detailed in Section II. The super-resolution auto-paired joint azimuth-range-Doppler estimator is developed in Section III. In Section IV, the derivation of a low complexity sequential framework is presented, along with discussion of complexity. Simulation and experimental results are presented in Section V and Section VI, respectively. Conclusions are given in Section VII.

***Notation:*** Bold lowercase letters, bold uppercase letters, and bold calligraphic letters denote column vectors, matrices, and tensors, respectively. We use: $\mathbb{C}^{m\times n}$ for $m \times n$ complex space; $(\cdot)^*$, $(\cdot)^\top$, $(\cdot)^{\mathrm{H}}$, $(\cdot)^{-1}$ for conjugate, transpose, conjugate transpose, and inverse; $\boldsymbol{A} \otimes \boldsymbol{B}$, $\boldsymbol{A} \odot \boldsymbol{B}$, $\boldsymbol{A} \circ \boldsymbol{B}$ for Kronecker, Khatri-Rao, and Hadamard products; $\boldsymbol{A}[m, n]$ for the $(m, n)$-th element of $\boldsymbol{A}$, $\boldsymbol{I}_K$ for $K \times K$ identity; $\mathrm{rect}(\cdot)$, $\mathrm{vec}(\cdot)$, $\mathrm{diag}(x)$, $\arg(\cdot)$ for rectangular function, column-wise vectorization, diagonal matrix, and complex argument.

## II. Models and Problem Statement

Consider a monostatic multiple-antenna OFDM sensing system. The transmitter emits the OFDM signals with communication capabilities, which is known at the receiver. The receiver is equipped with a uniform linear array (ULA) of $K$ antennas and is assumed to be well calibrated. We assume ideal synchronization and sufficient isolation between the transmitting antennas and the receiver. Furthermore, to avoid phase ambiguity, the uniform inter-element spacing $d$ between two adjacent sensors satisfies $d \leq \lambda/2$ with $\lambda = c/f_c$, where $c$ is the speed of light and $f_c$ is the carrier frequency.

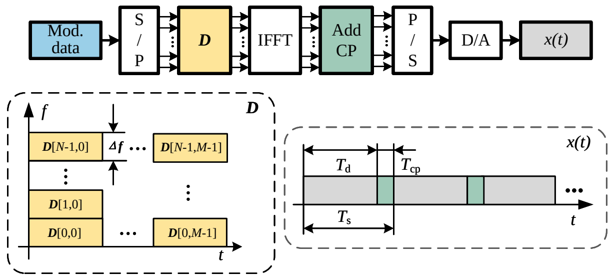


Fig. 1. Process of the modulation of OFDM baseband signals with $N$ subcarriers and $M$ symbols, where S/P, P/S, and D/A refers to serial to parallel conversion, parallel to serial conversion, and digital to analog conversion, respectively.

### A. Model of Transmit OFDM Signal

An OFDM signal consisting of $N$ orthogonal subcarriers with equal frequency spacing $\Delta f$ is considered, resulting in a total bandwidth of $B = N\Delta f$. The number of OFDM symbols utilized within a coherent processing interval (CPI) for sensing is denoted as $M$. The CPI refers to the time period over which signals are processed coherently to improve detection and measurement accuracy [2].

Fig. 1 illustrates the modulation process of OFDM signals. Here, $\mathbf{D} \in \mathbb{C}^{N\times M}$ denotes the transmitted modulation data matrix, which is composed of elements taken from a phase shift keying or quadrature amplitude modulation constellation. Besides, $\mathbf{D}$ is known to the receiver. Now, the time domain baseband OFDM signal is described as

$$x(t) = \sum_{m=0}^{M-1}\sum_{n=0}^{N-1} \mathbf{D}[n,m]\, e^{j2\pi n\Delta f(t-mT_{\mathrm{s}})} \mathrm{rect}\left(\frac{t-mT_{\mathrm{s}}}{T_{\mathrm{s}}}\right), \tag{1}$$

where $m = 0,1,\ldots,M-1$, $n = 0,1,\ldots,N-1$. The duration of a complete OFDM symbol is denoted as $T_{\mathrm{s}} = T_{\mathrm{d}} + T_{\mathrm{cp}}$, where $T_{\mathrm{d}} = 1/\Delta f$ represents the elementary symbol period, and $T_{\mathrm{cp}}$ is the duration of the cyclic prefix (CP). The CP is a repeated preamble sequence appended to OFDM symbols, is truncated and removed at the receiver based on the known length [14]. The function $\mathrm{rect}(t)$ represents a rectangular window function, which is equal to 1 between $-T_{\mathrm{cp}} < t < T_{\mathrm{d}}$ and otherwise constantly 0.

### B. Model of Measurement Signal

Assuming that the transmitted signal is reflected by $L$ point-like targets located at azimuth of arrival $\theta_l$, with range $r_l$ and radial velocity $v_l$ relative to the colocated receiving antennas, $l = 1,2,\ldots,L$. All targets are assumed to satisfy the far-field condition, given by $r_l \geq 2d^2/\lambda$ [31]. For simplicity, in this paper, steering vectors are defined as a combination of phase rotation $\zeta$ and vector length $U$ in Vandermonde form as

$$\boldsymbol{\alpha}(\zeta,U) \triangleq [1,\zeta^1,\zeta^2,\cdots,\zeta^{(U-1)}]^\top. \tag{2}$$

Considering an additive noise channel, the baseband received signal for a ULA can be represented in vector form as

$$\mathbf{y}(t) = \sum_{l=1}^{L}\boldsymbol{\alpha}(\zeta_{\theta_l},K)\beta_l x(t-\tau_l)e^{j2\pi f_{\mathrm{D}l}t} + \mathbf{z}(t) \tag{3}$$

with

$$\zeta_\theta \triangleq e^{j2\pi d\sin\theta/\lambda}, \tag{4}$$

where $\beta_l$ represents the reflectivity factor of the $l$-th target, $\tau_l = 2r_l/c$ denotes the propagation delay, $f_{\mathrm{D}l} = 2f_c v_l/c$ denotes the Doppler frequency shift, and $\mathbf{z}(t)$ is an additive noise vector.

According to the OFDM symbol period, $\mathbf{y}(t)$ can be divided into $M$ time segments, with each segment containing the original samples of one symbol [13]. Assuming a sampling rate $f_s = B$ and the CP is removed from each segment, the sample from the $m$-th symbol period can be expressed in matrix form $\mathbf{Y}_m \in \mathbb{C}^{K\times N}$, whose elements are given by

$$\begin{aligned}\mathbf{Y}_m[k,q] = \sum_{l=1}^{L}\sum_{n=0}^{N-1}\beta_l\mathbf{D}[n,m]\zeta_{\theta_l}^k e^{j2\pi n\Delta f(q/f_s-\tau_l)}\\ \cdot e^{j2\pi f_{Dl}(q/f_s+mT_s)} + \mathbf{Z}_m[k,q],\end{aligned} \tag{5}$$

where $k = 0,1,\ldots,K-1$, $q = 0,1,\ldots,N-1$, $\mathbf{Z}_m$ represents the sampling matrix of the $m$-th segment of $\mathbf{z}(t)$. In (5), $e^{j2\pi q f_{Dl}/f_s} \approx 1$ since $f_{Dl} \ll f_s$ [23] [32]. Thus, (5) can be approximated as

$$\begin{aligned}\mathbf{Y}_m[k,q] \approx \sum_{l=1}^{L}\sum_{n=0}^{N-1}\beta_l\mathbf{D}[n,m]\zeta_{\theta_l}^k\zeta_{\tau_l}^n\zeta_{f_{\mathrm{D}l}}^m e^{j2\pi n\Delta f q/f_s}\\ + \mathbf{Z}_m[k,q]\end{aligned} \tag{6}$$

with

$$\zeta_\tau \triangleq e^{-j2\pi\Delta f\tau}, \tag{7}$$

$$\zeta_{f_{\mathrm{D}}} \triangleq e^{j2\pi T_s f_{\mathrm{D}}}. \tag{8}$$

Under the assumption $f_{Dl} \ll f_s$, (5) can be interpreted as assuming that the Doppler frequency shift is approximately constant over each symbol period, leading to the approximation in (6). The columns of the $m$-th symbol sampled matrix $\mathbf{Y}_m$ represent multi-antenna data, while the rows correspond to complex samples in the fast-time domain.

### C. Model of Reconstructed OFDM Signal

We define $\mathrm{FFT}_n(\mathbf{A},N)$ as performing $N$-point fast Fourier transform (FFT) on the $n$-th dimension of $\mathbf{A}$. Follow the principles of OFDM demodulation [14], the recovered frequency-domain signal $\mathbf{S}_m \in \mathbb{C}^{K\times N}$ can be obtained by performing the FFT along the columns of $\mathbf{Y}_m$ as

$$\begin{aligned}\mathbf{S}_m &= \mathrm{FFT}_2(\mathbf{Y}_m,N)\\ &= \sum_{l=1}^{L}\boldsymbol{\alpha}(\zeta_{\theta_l},K)\beta_l\zeta_{f_{\mathrm{D}l}}^m\{\boldsymbol{\alpha}(\zeta_{\tau_l},N)\circ\mathbf{D}[:,m]\}^\top + \mathbf{Z}'_m,\end{aligned} \tag{9}$$

where $\mathbf{Z}'_m \in \mathbb{C}^{K\times N}$ is the corresponding noise matrix in the frequency domain. Here, $\mathbf{D}[:,m]$ represents the $m$-th column of matrix $\mathbf{D}$.

Since $\mathbf{D}$ is known to the receiver, the transmitted data embedded within each element $\mathbf{S}_m[k,n]$ can be effectively removed by comparing it with $\mathbf{D}$. For ease of representation, we stack the element-wise division matrices from each OFDM symbol to form a 3D-tensor $\boldsymbol{\mathcal{F}} \in \mathbb{C}^{K\times N\times M}$, referred to as the reconstructed data cube. The $(k,n,m)$-th element in $\boldsymbol{\mathcal{F}}$ can be expressed as

$$\begin{aligned}\boldsymbol{\mathcal{F}}[k,n,m] &= \mathbf{S}_m[k,n]/\mathbf{D}[n,m] \\ &= \sum_{l=1}^{L} \beta_l \zeta_{\theta_l}^{k} \zeta_{\tau_l}^{n} \zeta_{f_{\mathrm{D}l}}^{m} + \boldsymbol{\mathcal{Z}}[k,n,m],\end{aligned} \tag{10}$$

where the elements within $\boldsymbol{\mathcal{Z}} \in \mathbb{C}^{K\times N\times M}$ are derived by dividing each $\mathbf{Z}'_m[k,n]$ by the corresponding element in $\mathbf{D}[n,m]$. As shown in (10), the model corresponds to a classical multi-dimensional harmonic retrieval formulation, where the target states are encoded in the phase rotations along each dimension, as characterized by (4), (7), and (8).

### *D. Problem Statement*

In this paper, we focus on parameter estimation from the reconstructed baseband OFDM echo, represented as a data cube $\boldsymbol{\mathcal{F}}$. Existing super-resolution techniques mainly follow two paths: (i) applying digital beamforming (DBF) to form azimuth-specific streams before range-Doppler estimation [19], [21], [23], where angular resolution is limited by the array aperture; or (ii) estimating angles first, then extracting range-Doppler parameters [17], [24], [33], where statistical averaging over OFDM snapshots hinders accurate recovery.

A potential alternative is to match single-beam range-Doppler estimates with high-resolution angle estimates. However, in multi-target scenarios this causes identification ambiguity, as illustrated in Fig. 2, where intersections of estimated ranges and angles generate multiple hypotheses, complicating target discrimination.

As illustrated in Fig. 3, after DFT and point-wise division, the OFDM measurements can be reorganized into a structured 3D data cube along the antenna, subcarrier, and symbol dimensions. In this reconstructed cube, angle, range, and Doppler manifest as separable phase rotations across the axes, forming a Kronecker-type harmonic structure. Such separability naturally enables harmonic parameter extraction methods, including propagator-based approaches, to be extended to multi-dimensional parameter estimation.

Based on this structured model, subspace-based joint estimation methods [25], [26] have been developed to estimate the parameters by exploiting eigen-decomposed signal-noise subspaces. However, these approaches incur high computational cost. For example, in a 5G NR system with 30 kHz subcarrier spacing, $B = 5,$MHz bandwidth, and a 16-element array over one slot (14 OFDM symbols), the data cube is $\boldsymbol{\mathcal{F}} \in \mathbb{C}^{16\times 132\times 14}$, leading to a complexity of $10^{13} \sim 10^{14}$ floating-point operations (FLOPs). In larger deployments, such as mmWave with thousands of subcarriers and massive arrays, the burden is even greater, making such methods impractical for embedded or edge devices.

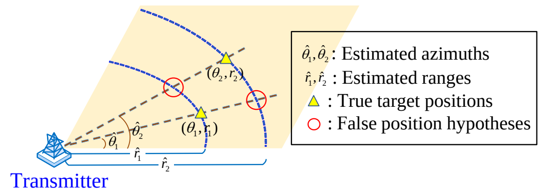


Fig. 2. The identification ambiguity problem in angle-range estimation. For two targets in the figure, randomly matching two azimuths estimates with two range estimates results in four potential location hypotheses, making it difficult to identify the true target positions.

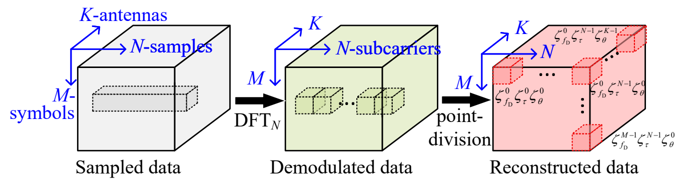


Fig. 3. Illustration of the reconstructed OFDM data cube formation. After DFT and point-wise division, the sampled data are reorganized into a structured 3D cube, where $\zeta_\theta$, $\zeta_\tau$, and $\zeta_{f_{\mathrm{D}}}$ represent the phase terms induced by angle, delay, and Doppler, respectively (ignoring amplitude attenuation).

## III. Super-Resolution Joint Azimuth-Range-Doppler Estimator

In this section, we derive a super-resolution estimator for joint azimuth-range-Doppler estimation of multiple targets. The received data $\boldsymbol{\mathcal{F}}$ is vectorized to reformulate the problem as multivariate phase rotation estimation. Forward-backward smoothing is then applied to mitigate snapshot correlation, and an extended propagator is constructed to approximate the noise subspace without costly eigenvalue decomposition while preserving high estimation accuracy.

### *A. Data Vectorization*

The spurious target hypotheses in Fig. 2 result from processing echoes independently across different dimensions. To enable unified multidimensional processing, vectorization arranges a matrix or tensor into a vector in a specific order. Using the Vandermonde form in (2), $\boldsymbol{\mathcal{F}}$ is vectorized sequentially over symbols, subcarriers, and array elements, yielding a vector of length $KMN$ as

$$\mathrm{vec}(\boldsymbol{\mathcal{F}}) = \sum_{l=1}^{L} \beta_l \boldsymbol{\alpha}(\zeta_{\theta_l}, K) \otimes \boldsymbol{\alpha}(\zeta_{\tau_l}, N) \otimes \boldsymbol{\alpha}(\zeta_{f_{\mathrm{D}l}}, M) + \mathrm{vec}(\boldsymbol{\mathcal{Z}}). \tag{11}$$

Now, the cross-dimensional parameter estimation problem is reformulated as estimating the phase rotations $\zeta_{\theta_l}$, $\zeta_{\tau_l}$, and $\zeta_{f_{\mathrm{D}l}}$ of multivariate steering vectors in a unified dimension. Since all target phase rotations appear within the same snapshot in (11), the target echoes become fully correlated, hindering subspace separation and parameter estimation. To alleviate this, we apply forward-backward smoothing [34] as a preprocessing step, which generates multi-snapshot data and incorporates the Kronecker-structured phase rotations for decorrelation.

### *B. Forward-Backward Smoothing in Azimuth-Range-Doppler Domain*

First, the size of the forward smoothing window is defined as $\bar{K}\times\bar{N}\times\bar{M}$, where $\bar{K}$, $\bar{N}$, and $\bar{M}$ are adjustable based on specific application requirements. For the 2D case, a quasi-optimal setting is detailed in [32]. Let $\tilde{K}\triangleq K-\bar{K}+1$, $\tilde{N}\triangleq N-\bar{N}+1$, $\tilde{M}\triangleq M-\bar{M}+1$, then $\tilde{W}=\tilde{K}\tilde{N}\tilde{M}$ represents the total number of forward observations after smoothing. Each observation, referred to as a sub-data-cube, is defined as

$$\bar{\boldsymbol{\mathcal{F}}}_{\tilde{k},\tilde{n},\tilde{m}}\triangleq\boldsymbol{\mathcal{F}}[\tilde{k}:\tilde{k}+\bar{K}-1,\tilde{n}:\tilde{n}+\bar{N}-1,\tilde{m}:\tilde{m}+\bar{M}-1], \tag{12}$$

where $\tilde{k}=0,1,\ldots,\tilde{K}-1$, $\tilde{n}=0,1,\ldots,\tilde{N}-1$, $\tilde{m}=0,1,\ldots,\tilde{M}-1$. For simplicity, the Kronecker product component of the steering vector is omitted, and the smoothed steering vectors, with and without the true target parameters, are defined as

$$\bar{\boldsymbol{\alpha}}\triangleq\boldsymbol{\alpha}(\zeta_\theta,\bar{K})\otimes\boldsymbol{\alpha}(\zeta_\tau,\bar{N})\otimes\boldsymbol{\alpha}(\zeta_{f_\mathrm{D}},\bar{M}), \tag{13}$$

$$\bar{\boldsymbol{\alpha}}_l\triangleq\boldsymbol{\alpha}(\zeta_{\theta_l},\bar{K})\otimes\boldsymbol{\alpha}(\zeta_{\tau_l},\bar{N})\otimes\boldsymbol{\alpha}(\zeta_{f_{\mathrm{D}l}},\bar{M}), \tag{14}$$

$$\tilde{\boldsymbol{\alpha}}_l\triangleq\boldsymbol{\alpha}(\zeta_{\theta_l},\tilde{K})\otimes\boldsymbol{\alpha}(\zeta_{\tau_l},\tilde{N})\otimes\boldsymbol{\alpha}(\zeta_{f_{\mathrm{D}l}},\tilde{M}). \tag{15}$$

Then, by vectorizing $\bar{\boldsymbol{\mathcal{F}}}$ sequentially along the dimensions of array elements, subcarriers, and symbols, one of the $\tilde{W}$ snapshots is obtained as

$$\begin{aligned}\mathbf{g}_{\tilde{k},\tilde{n},\tilde{m}}&=\mathrm{vec}(\bar{\boldsymbol{\mathcal{F}}}_{\tilde{k},\tilde{n},\tilde{m}})\\&=\sum_{l=1}^{L}\zeta_{\theta_l}^{\tilde{k}}\zeta_{\tau_l}^{\tilde{n}}\zeta_{f_{\mathrm{D}l}}^{\tilde{m}}\beta_l\bar{\boldsymbol{\alpha}}_l+\mathrm{vec}(\bar{\boldsymbol{\mathcal{Z}}}_{\tilde{k},\tilde{n},\tilde{m}}),\end{aligned} \tag{16}$$

where $\bar{\boldsymbol{\mathcal{Z}}}_{\tilde{k},\tilde{n},\tilde{m}}$ is derived from $\boldsymbol{\mathcal{Z}}$ in the same way that $\bar{\boldsymbol{\mathcal{F}}}_{\tilde{k},\tilde{n},\tilde{m}}$ is defined from $\boldsymbol{\mathcal{F}}$. The vector snapshot $\mathbf{g}_{\tilde{k},\tilde{n},\tilde{m}}\in\mathbb{C}^{\bar{W}}$ has a length of $\bar{W}=\bar{K}\bar{N}\bar{M}$.

Next, the $\tilde{W}$ snapshots are sorted by indices $\tilde{k}$, $\tilde{m}$, and $\tilde{n}$ in ascending order and concatenated column-wise to form a new forward smoothing observation as

$$\begin{aligned}\mathbf{G}_\mathrm{f}&=[\mathbf{g}_{0,0,0},\mathbf{g}_{0,0,1},\cdots,\mathbf{g}_{\tilde{k},\tilde{n},\tilde{m}},\cdots,\mathbf{g}_{\tilde{K}-1,\tilde{N}-1,\tilde{M}-1}]\\&=\bar{\mathbf{A}}\mathbf{B}\tilde{\mathbf{A}}^\top+\bar{\mathbf{Z}},\end{aligned} \tag{17}$$

where

$$\bar{\mathbf{A}}=[\bar{\boldsymbol{\alpha}}_1,\bar{\boldsymbol{\alpha}}_2,\cdots,\bar{\boldsymbol{\alpha}}_L], \tag{18}$$

$$\tilde{\mathbf{A}}=[\tilde{\boldsymbol{\alpha}}_1,\tilde{\boldsymbol{\alpha}}_2,\cdots,\tilde{\boldsymbol{\alpha}}_L], \tag{19}$$

$$\mathbf{B}=\mathrm{diag}\left(\beta_1,\beta_2,\cdots,\beta_L\right), \tag{20}$$

and $\bar{\mathbf{Z}}$ is formed by combining $\mathrm{vec}(\bar{\boldsymbol{\mathcal{Z}}}_{\tilde{k},\tilde{n},\tilde{m}})$ for all $\tilde{k},\tilde{n},\tilde{m}$.

In (17), forward smoothing reduces the correlation between echoes from different targets. Beyond forward smoothing, forward-backward smoothing [35] further enhances the decorrelation. It utilizes both forward and backward observations, effectively doubling the number of available snapshots [34]. Since the observation matrix (17) is already expressed in a unified steering vector form, let $\mathbf{J}_n$ denote an $n\times n$ reversal matrix with ones on its anti-diagonal and zeros elsewhere. The backward smoothing observation matrix can then be computed as

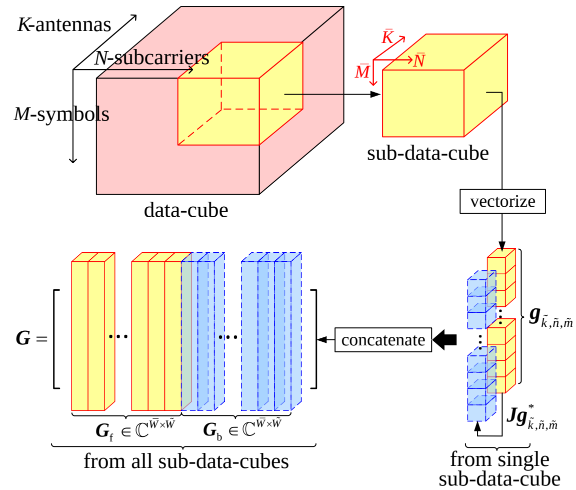


Fig. 4. Data smoothing in azimuth-range-Doppler domain.

$$\begin{aligned}\mathbf{G}_\mathrm{b}=&\mathbf{J}_{\bar{W}}\mathbf{G}_\mathrm{f}^*\\=&\mathbf{J}_{\bar{W}}\bar{\mathbf{A}}^*\mathbf{B}^*\tilde{\mathbf{A}}^\mathrm{H}+\mathbf{J}_{\bar{W}}\bar{\mathbf{Z}}^*\\=&\bar{\mathbf{A}}\bar{\mathbf{B}}\tilde{\mathbf{A}}^\mathrm{H}+\mathbf{J}_{\bar{W}}\bar{\mathbf{Z}}^*,\end{aligned} \tag{21}$$

where

$$\bar{\mathbf{B}}=\mathrm{diag}\left([\beta_1^*\zeta_{\theta_1}^{1-\bar{K}}\zeta_{\tau_1}^{1-\bar{N}}\zeta_{f_{\mathrm{D}1}}^{1-\bar{M}},\cdots,\beta_L^*\zeta_{\theta_L}^{1-\bar{K}}\zeta_{\tau_L}^{1-\bar{N}}\zeta_{f_{\mathrm{D}L}}^{1-\bar{M}}]\right). \tag{22}$$

The matrix $\mathbf{G}_\mathrm{b}$ has an identical steering vector matrix to that of $\mathbf{G}_\mathrm{f}$. Using the forward-backward snapshots, the smoothed observation matrix can be concatenated as

$$\mathbf{G}=\left[\mathbf{G}_\mathrm{f},\mathbf{G}_\mathrm{b}\right]. \tag{23}$$

The data smoothing in the azimuth-range-Doppler domain is illustrated in Fig. 4.

Forward-backward smoothing improves decorrelation by constructing sub-data-cubes of size $\bar{K}\bar{N}\bar{M}$, whose steering vectors are given in (13). Since $\bar{K}\le K$, $\bar{N}\le N$, and $\bar{M}\le M$, the effective aperture and physical degrees of freedom are correspondingly reduced, which may affect the achievable resolution. Moreover, smoothing assumes quasi-stationarity within a CPI. If targets exhibit noticeable motion such that (6) is violated, the separable harmonic structure in (16) may not strictly hold, thereby weakening the decorrelation effect and degrading the estimation accuracy.

### *C. Joint Estimation with Extended Orthonormal Propagator*

Utilizing the observation matrix in a unified steering vector form, a common approach is to compute the covariance matrix and apply eigenvalue decomposition (EVD) to obtain the corresponding noise subspace eigenvectors of the signal. Super-resolution algorithms, such as MUSIC [36], can then be used for parameter estimation. However, as the size of the observation scales as $O(KMN)$ with the data dimensionality, and the complexity of covariance matrix calculation and EVD scales with the cube of the number of equivalent elements, such an approach becomes computationally expensive.

To avoid computationally intensive eigenvalue calculations, and to leverage the orthogonality of subspaces for estimation, we propose to extend the propagator method from DOA estimation [30] to achieve 3D phase rotations estimation. This method constructs the noise subspace and estimates phase rotations in the steering vectors using a linear operator without implementing covariance matrix calculation or EVD.

**Definition 1.** *For matrix $\mathbf{X} \in \mathbb{C}^{M\times N}$, $M > N$, the propagator $\mathbf{P}_{\mathrm{x}} \in \mathbb{C}^{N\times(M-N)}$ is defined as*

$$\mathbf{X}_2 = \mathbf{P}_{\mathrm{x}}^H \mathbf{X}_1, \tag{24}$$

*where $\mathbf{X}_1 \in \mathbb{C}^{N\times N}$ and $\mathbf{X}_2 \in \mathbb{C}^{(M-N)\times N}$ called submatrices are obtained by partitioning $\mathbf{X}$ as*

$$\mathbf{X} = [\overbrace{\mathbf{X}_1^\top}^{N}, \overbrace{\mathbf{X}_2^\top}^{M-N}]^\top, \tag{25}$$

*and $\mathbf{X}_1$ is non-singular. The above definition is equivalent to*

$$\mathbf{X}^H \mathbf{Q}_{\mathrm{x}} = \mathbf{0}_{N\times(M-N)}, \tag{26}$$

$$\mathbf{Q}_{\mathrm{x}} = [\mathbf{P}_{\mathrm{x}}{}^\top, -\mathbf{I}_{M-N}]^\top, \tag{27}$$

*where $\mathbf{0}_{m\times n}$ represent null matrix of dimension $m \times n$.*

According to Definition 1, propagator-based estimation framework relies on partitioning the observation or steering matrix to construct a linear representation between submatrices. In the one-dimensional case, the Vandermonde steering vector is driven by a single phase parameter, allowing a simple row-wise split as in (25) to preserve full column rank. Thus supports the stable and unique linear representation [37].

However, in multidimensional models, such as the Kronecker-structured steering vector in (18), multiple phase rotations jointly determine the response along distinct dimensions. A naive selection of the first $L$ rows may only capture observations from a subset of dimensions. In such cases, without sufficient separability in subcarrier-induced phase rotations across targets, the submatrices may lose full column rank.

To make this issue precise, we adopt a notation that is independent of the specific vectorization order. Let the lengths of the steering vectors along each dimension be denoted by $\bar{U}_d$, $d = 1, 2, 3$. For example, according to the vectorization order in (11), we have

$$\{\bar{U}_d \mid \bar{U}_1 = \bar{K}, \bar{U}_2 = \bar{N}, \bar{U}_3 = \bar{M}\}. \tag{28}$$

Under any fixed Kronecker-consistent order, selecting the first $L$ rows exhausts lower-order dimensions before higher-order ones, which leads to the following result.

**Proposition 1.** *Form the submatrix $\bar{\mathbf{A}}_1 \in \mathbb{C}^{L\times L}$ by selecting the* first *$L$ rows of $\bar{\mathbf{A}}$ according to any fixed Kronecker-consistent vectorization order. Define*

$$\delta(L) \triangleq \max\Big\{ j \in \{1,2,3\} : \ L \le \prod_{d=1}^{j} \bar{U}_d \Big\}. \tag{29}$$

*If $\delta(L) < 3$, then the mapping from the full 3D parameter set to the columns of $\bar{\mathbf{A}}_1$ is non-injective, and $\bar{\mathbf{A}}_1$ cannot, in general, be guaranteed to have full column rank.*

*Proof.* See Appendix A. □

Proposition 1 reveals that rank deficiency arises not from the propagator framework itself, but from the implicit coupling between the submatrix construction and the vectorization order. To prevent such degeneracy, it is therefore necessary to decouple the subarray selection process from the inherent ordering of the vectorized data and instead revert to the underlying physical geometry of the array. Specifically, the submatrix should be constructed by selecting row indices from the steering matrix that are non-collinear and non-coplanar across multiple observational dimensions, thereby ensuring that inter-source phase variations along all dimensions are sufficiently captured.

Defining a structured index space as

$$\mathcal{I} = \big\{ \boldsymbol{i} = (u_1, u_2, u_3) \,\big|\, 1 \le u_d \le \bar{U}_d,\ d = 1,2,3 \big\}. \tag{30}$$

Let $\kappa : \mathcal{I} \to \{1, 2, \ldots, \bar{K}\bar{N}\bar{M}\}$ denote a bijective mapping from the multidimensional index space to the vectorized row index of the steering matrix, defined as:

$$\kappa(u_1, u_2, u_3) = (u_1 - 1)\bar{U}_2\bar{U}_3 + (u_2 - 1)\bar{U}_3 + u_3 \tag{31}$$

**Theorem 1.** *Select a subset $\mathcal{S} \subset \mathcal{I}$ with $|\mathcal{S}| = \max(L, 4)$, and form the submatrix*

$$\bar{\mathbf{A}}_1 = \bar{\mathbf{A}}[\kappa(\mathcal{S}), :] \in \mathbb{C}^{L\times L}. \tag{32}$$

*If the affine dimension of $\mathcal{S}$ equal to 3, i.e., there exist four distinct points $\boldsymbol{i}_1, \boldsymbol{i}_2, \boldsymbol{i}_3, \boldsymbol{i}_4 \in \mathcal{S}$ such that*

$$(\boldsymbol{i}_2 - \boldsymbol{i}_1) \times (\boldsymbol{i}_3 - \boldsymbol{i}_1) \ne \mathbf{0}, \tag{33}$$

$$\big[(\boldsymbol{i}_2 - \boldsymbol{i}_1) \times (\boldsymbol{i}_3 - \boldsymbol{i}_1)\big] \cdot (\boldsymbol{i}_4 - \boldsymbol{i}_1) \ne 0, \tag{34}$$

*then $\det(\bar{\mathbf{A}}_1)$ is a nonzero multivariate polynomial in $\{(\zeta_{\theta_l}, \zeta_{\tau_l}, \zeta_{f_{\mathrm{D}l}})\}_{l=1}^{L}$. Consequently, $\bar{\mathbf{A}}_1$ is nonsingular and has full column rank for generic target parameters.*

*Proof.* See Appendix B. □

Theorem 1 provides a geometric condition under which the selected submatrix $\bar{\mathbf{A}}_1$ is generically full rank. Specifically, (33)–(34) ensure that the index set $\mathcal{S}$ preserves 3D phase variation, so that rank deficiency can occur only for a measure-zero set of pathological parameter configurations. This stands in contrast to Proposition 1, where insufficient affine dimensionality leads to structural rank loss over entire parameter dimensions.

Moreover, since the dimensionality of the inter-source phase variations is not known a priori, it is advisable to preset $|\mathcal{S}| \ge 4$ even when the number of sources is less than four.

**Remark 1.** *Although various strategies can be employed for selecting $\mathcal{S}$, a simple yet effective approach is to first choose an arbitrary vertex of the cube, and then randomly select $L - 1$ additional indices along the three edges or three faces connected to it. This procedure largely mitigates the possibility of collinearity or coplanarity among the selected indices.*

Given a subset $\mathcal{S} \subset \mathcal{I}$ with affine dimension equal to 3 and cardinality $|\mathcal{S}| = L$, the extended propagator under affine index selection is defined as follows.

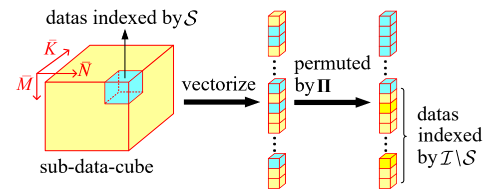


Fig. 5. Index selection and permutation using a single snapshot.

**Definition 2.** *Let $\bar{\mathbf{A}} \in \mathbb{C}^{\bar{W}\times L}$ be an steering matrix with Kronecker-product structure. The extended propagator $\mathbf{P} \in \mathbb{C}^{L\times(\bar{W}-L)}$ is defined as*

$$\bar{\mathbf{A}}_2 = \mathbf{P}^{\mathrm{H}}\bar{\mathbf{A}}_1, \tag{35}$$

*where the submatrices $\bar{\mathbf{A}}_1 \in \mathbb{C}^{L\times L}$ and $\bar{\mathbf{A}}_2 \in \mathbb{C}^{(\bar{W}-L)\times L}$ are obtained by partitioning $\bar{\mathbf{A}}$ as*

$$\bar{\mathbf{A}}_1 = \bar{\mathbf{A}}[\kappa(\mathcal{S}), :], \quad \bar{\mathbf{A}}_2 = \bar{\mathbf{A}}[\kappa(\mathcal{I}\setminus\mathcal{S}), :]. \tag{36}$$

*The above definition is well posed since $\bar{\mathbf{A}}_1$ is nonsingular.*

However, in contrast to the classical propagator, the extended propagator cannot directly be used to construct orthogonal functions as in (26), since the affine index selection of the subarray does not follow the vectorization order used to construct the steering matrix. To enable a subspace-based orthogonality representation, we introduce a row permutation matrix as

$$\mathbf{\Pi} = \begin{bmatrix} \mathbf{I}_{\bar{W}}[\kappa(\mathcal{S}), :] \\ \mathbf{I}_{\bar{W}}[\kappa(\mathcal{I}\setminus\mathcal{S}), :] \end{bmatrix}. \tag{37}$$

**Corollary 1.** *Given the extended propagator $\mathbf{P}$ and the row permutation matrix $\mathbf{\Pi}$, define*

$$\mathbf{Q}_{\mathrm{a}} = \left[\mathbf{P}^{\top},\ -\mathbf{I}_{\bar{W}-L}\right]^{\top}, \tag{38}$$

*the following orthogonality condition holds:*

$$\begin{aligned} \bar{\mathbf{A}}^{\mathrm{H}}\mathbf{Q} &= (\mathbf{\Pi}\bar{\mathbf{A}})^{\mathrm{H}}\mathbf{Q}_{\mathrm{a}} \\ &= [\bar{\mathbf{A}}_1^{\mathrm{H}},\ \bar{\mathbf{A}}_2^{\mathrm{H}}]\mathbf{Q}_{\mathrm{a}} \\ &= \mathbf{0}_{L\times(\bar{W}-L)}, \end{aligned} \tag{39}$$

*where*

$$\mathbf{Q} = \mathbf{\Pi}^{\mathrm{H}}\mathbf{Q}_{\mathrm{a}}. \tag{40}$$

Corollary 1 implies that the columns of $\mathbf{Q}$ lie in the noise subspace orthogonal to the steering vectors. Fig. 5 illustrates index selection and permutation for a single sub-data-cube. After determining $S$, the submatrix indices are irregularly embedded in the columns of $\mathbf{A}$, as shown in (31). A permutation is then applied to make the resulting partitioning conform to the standard propagator form in (25).

To estimate the extended propagator from the observation data, (23) is similarly partitioned as

$$\mathbf{G}_1 = \mathbf{G}[\kappa(\mathcal{S}), :], \quad \mathbf{G}_2 = \mathbf{G}[\kappa(\mathcal{I}\setminus\mathcal{S}), :]. \tag{41}$$

As with most subspace-based methods, the number of targets $L$ is equivalent to the model order and must be preset during partitioning. Several approaches have been proposed to estimate $L$ without resorting to EVD [38], [39]. In the following analysis, $L$ is assumed to have been estimated and preset.

Even when $L$ is unknown, the propagator can still be constructed by assuming a target number, owing to the inevitable presence of noise in the data [37].The impact of model-order settings on performance will be demonstrated in Section V-C.

In addition, even if the linear independence of steering vectors and the non-degeneracy of the selected submatrices are satisfied, the propagator method differs from covariance-based approaches in that it does not explicitly construct and average second-order statistics. Instead, estimation relies on the structured data model. Consequently, in low-signal-to-noise ratio (SNR) or small-sample regimes, it may be more sensitive to noise perturbations than methods that exploit explicit signal-noise subspace separation, such as MUSIC [25].

Given that $\mathbf{G}_1$ is full column rank, the corresponding propagator can be obtained by minimizing the following cost function:

$$\min_{\mathbf{P}} \|\mathbf{G}_2 - \mathbf{P}^{\mathrm{H}}\mathbf{G}_1\|_{\mathrm{F}}^2, \tag{42}$$

where $\|\cdot\|_{\mathrm{F}}$ represents the Frobenius norm. The optimization in (42) is equivalent to solving a convex problem for each element of $\mathbf{P}$, with the optimal solution given by

$$\hat{\mathbf{P}} = \left(\mathbf{G}_1\mathbf{G}_1^{\mathrm{H}}\right)^{-1}\mathbf{G}_1\mathbf{G}_2^{\mathrm{H}}. \tag{43}$$

The projection matrix is computed according to (40) and (38) as

$$\hat{\mathbf{Q}} = \mathbf{\Pi}^{\mathrm{H}}\left[\hat{\mathbf{P}}^{\top}, -\mathbf{I}_{\bar{W}-L}\right]^{\top}. \tag{44}$$

Then, the following orthonormalized spectrum function is constructed as

$$\rho(\theta,\tau,f_{\mathrm{D}}) = \frac{1}{\bar{\boldsymbol{\alpha}}^{\mathrm{H}}\hat{\mathbf{Q}}(\hat{\mathbf{Q}}^{\mathrm{H}}\hat{\mathbf{Q}})^{-1}\hat{\mathbf{Q}}^{\mathrm{H}}\bar{\boldsymbol{\alpha}}}. \tag{45}$$

The orthonormalization of the matrix $\hat{\mathbf{Q}}$ in (45) enhances the projection of the steering matrix onto the noise subspace, thereby improving estimation performance [30]. Furthermore, due to the special structure introduced by the permutation, $(\hat{\mathbf{Q}}^{\mathrm{H}}\hat{\mathbf{Q}})^{-1}$ can be efficiently computed using the matrix inversion lemma as

$$\begin{aligned} (\hat{\mathbf{Q}}^{\mathrm{H}}\hat{\mathbf{Q}})^{-1} &= (\hat{\mathbf{Q}}_{\mathrm{a}}^{\mathrm{H}}\mathbf{\Pi}\mathbf{\Pi}^{\mathrm{H}}\hat{\mathbf{Q}}_{\mathrm{a}})^{-1} \\ &= (\hat{\mathbf{Q}}_{\mathrm{a}}^{\mathrm{H}}\hat{\mathbf{Q}}_{\mathrm{a}})^{-1} \\ &= \mathbf{I}_{\bar{W}-L} - \hat{\mathbf{P}}^{\mathrm{H}}(\mathbf{I}_L + \hat{\mathbf{P}}\hat{\mathbf{P}}^{\mathrm{H}})^{-1}\hat{\mathbf{P}}, \end{aligned} \tag{46}$$

where the computational complexity is reduced from $\mathcal{O}[\bar{W}(\bar{W}-L)^2]$ to $\mathcal{O}[L(\bar{W}-L)^2]$. Finding the $L$ largest peaks of (45) yields the optimal estimates for the respective parameters. We name this estimator the propagator-based joint azimuth-range-Doppler (PJ-ARD) estimator, which is summarized in Algorithm 1.

In the PJ-ARD estimator, the computational complexity of subspace calculation is $\mathcal{O}[\bar{W}^2 + L\bar{W}\tilde{W} + L(\bar{W}-L)^2]$, which is significantly lower than the $\mathcal{O}[\bar{W}^3 + \bar{W}^2\tilde{W}]$ complexity of EVD-based methods when $\bar{W} = \bar{K}\bar{N}\bar{M}$ is large [30]. However, calculating the spectrum function $\rho(\theta,\tau,f_{\mathrm{D}})$ in (45) involves the steering vector $\bar{\boldsymbol{\alpha}}$, which depends on three parameters to be estimated. Conducting a multidimensional grid search may pose a substantial computational burden. Achieving high precision in parameter estimation notably escalates computational complexity. In the next section, we propose a low-complexity alternative solution.

**Algorithm 1:** The Proposed PJ-ARD Estimator with Super-Resolution

**Input:** $\boldsymbol{\mathcal{F}} \in \mathbb{C}^{K\times N\times M}, \bar{K}, \bar{M}, \bar{N}, \Delta f, T_{\mathrm{s}}, \lambda, c, f_c, d.$

1. Perform azimuth-range-Doppler smoothing on $\boldsymbol{\mathcal{F}}$ as in (12), then vectorize all sub-data-cubes as in (16).
2. Construct $\boldsymbol{G}_{\mathrm{f}}$ and $\boldsymbol{G}_{\mathrm{b}}$ as in (17) and (21), then concatenate them to form $\boldsymbol{G}$ as in (23).
3. Estimate $L$ using methods from [38] or [39], and determine the set $\mathcal{S}$ that satisfies conditions (33) and (34).
4. Compute the corresponding mapped indices according to (28) and (31).
5. Partition $\boldsymbol{G}$ as in (41), compute the propagator estimates $\hat{\boldsymbol{P}}$ and $\hat{\boldsymbol{Q}}$ as in (43) and (44), respectively.
6. Calculate (45) according to the parameter grid and find the $L$ largest peaks. The corresponding coordinates $\hat{\theta}_l$, $\hat{r}_l$, and $\hat{v}_l$ are the estimates of azimuth, range, and velocity, respectively, for $l = 1, 2, \ldots, L$.

**Output:** $\hat{\theta}_l$, $\hat{r}_l$, $\hat{v}_l$.

## IV. Sequential Multiple Parameters Estimation Framework With Low Complexity

In this section, we present a sequential framework to reduce the computational complexity of the PJ-ARD estimator. Unlike the method in Section II-D, which may suffer from parameter mismatches across dimensions, the proposed approach first estimates specific parameters collectively for all targets, then performs an auto-matched joint estimation of the remaining parameters for each individual target. This design improves efficiency while ensuring consistent parameter matching across different dimensions.

First, we outline the general expression of the sequential estimation framework. Next, we propose a two-stage implementation based on the azimuth-range before Doppler model, incorporating the orthonormal propagator for efficient parameter estimation. Finally, we analyze the computational complexity of the sequential approach compare with PJ-ARD estimator.

### A. General Expression of Sequential Estimation Framework

The primary goal of this framework is to reduce the significant complexity associated with the multidimensional parameter search in the PJ-ARD estimator. To begin with, matrix unfolding (MUF), instead of vectorization in (11), is applied to the reconstructed data cube $\boldsymbol{\mathcal{F}}$. Standard MUF refers to the process of flattening a higher-order tensor along a specified dimension, explicitly representing part of the tensor structure in matrix form [28]. Unlike vectorization, MUF represents data from certain dimensions as multi-snapshot observations, rather than directly expressing all phase rotations in the steering vector. Note that the parameters $\theta_l, \tau_l, f_{\mathrm{D}l}$ to be estimated are embedded within the phase rotations generated by data alignment along the array, subcarrier, and symbol dimensions of $\boldsymbol{\mathcal{F}}$, respectively. Therefore, the corresponding parameters are used to represent the data dimensions, and two types of MUF for $\boldsymbol{\mathcal{F}}$ along the dimensions defined by one or two parameters are as follows:

**Definition 3.** *For reconstructed data cube $\boldsymbol{\mathcal{F}} \in \mathbb{C}^{K\times N\times M}$, the 1D-MUF is defined as*

$$MUF(\boldsymbol{\mathcal{F}}, \{\theta\}) = \mathbf{X}_1 \in \mathbb{C}^{K\times MN}, \tag{47}$$
$$MUF(\boldsymbol{\mathcal{F}}, \{\tau\}) = \mathbf{X}_2 \in \mathbb{C}^{N\times MK}, \tag{48}$$
$$MUF(\boldsymbol{\mathcal{F}}, \{f_D\}) = \mathbf{X}_3 \in \mathbb{C}^{M\times NK}, \tag{49}$$

*where $\mathbf{X}_1[k, nN+m] = \mathbf{X}_2[n, kK+m] = \mathbf{X}_3[m, kK+n] = \boldsymbol{\mathcal{F}}[k, n, m]$.*

**Definition 4.** *For reconstructed data cube $\boldsymbol{\mathcal{F}} \in \mathbb{C}^{K\times N\times M}$, the 2D-MUF is defined as*

$$MUF(\boldsymbol{\mathcal{F}}, \{\theta, \tau\}) = \mathbf{X}_{12} \in \mathbb{C}^{NK\times M} = \mathbf{X}_3^\top \tag{50}$$
$$MUF(\boldsymbol{\mathcal{F}}, \{\theta, f_D\}) = \mathbf{X}_{13} \in \mathbb{C}^{MK\times N} = \mathbf{X}_2^\top \tag{51}$$
$$MUF(\boldsymbol{\mathcal{F}}, \{\tau, f_D\}) = \mathbf{X}_{23} \in \mathbb{C}^{MN\times K} = \mathbf{X}_1^\top \tag{52}$$

*where $\mathbf{X}_{12}[kK+n, m] = \mathbf{X}_{13}[kK+m, n] = \mathbf{X}_{23}[nN+m, k] = \boldsymbol{\mathcal{F}}[k, n, m]$.*

In the following, we provide a unified representation of multiple parameters. The set of parameters of interest is defined as $\Theta = \{\xi_i \mid \xi_1 = \theta, \xi_2 = \tau, \xi_3 = f_D, i = 1, 2, 3\}$. The corresponding lengths of their steering vectors are given as $\{U_i \mid U_1 = K, U_2 = N, U_3 = M, i = 1, 2, 3\}$ before smoothing, and as (28) after smoothing. Without loss of generality, we divide the parameters contained in $\Theta$ into two parts. We define $\Psi$ as a proper subset of $\Theta$, and its complement $\Psi^{\mathrm{c}}$, such that

$$\Psi \subsetneq \Theta \quad \text{and} \quad \Psi^{\mathrm{c}} = \Theta \setminus \Psi. \tag{53}$$

The true value of $\Theta$, $\Psi$ and $\Psi^{\mathrm{c}}$ of the $l$-th target is denoted by $\Theta_l$, $\Psi_l$ and $\Psi_l^{\mathrm{c}}$, respectively.

*1) Estimation of $\Psi$ through MUF:* The first step of the sequential framework is to isolate $\Psi$ within $\Theta$ for pre-estimation. From Definitions 3 and 4, it can be observed that MUF essentially involves only a rearrangement of the data cube $\boldsymbol{\mathcal{F}}$. However, unlike vectorization, the MUF enables the corresponding steering vectors to adopt a more flexible, parameterized Kronecker product structure: once $\Psi$ is determined (the determination of $\Psi$ will be discussed in the next subsection), the MUF of $\boldsymbol{\mathcal{F}}$ can be expressed in the form of

$$\begin{aligned}\mathbf{F} &= \mathrm{MUF}(\boldsymbol{\mathcal{F}}, \Psi)\\ &= \sum_{l=1}^{L} \boldsymbol{\gamma}(\Psi_l)\beta_l \boldsymbol{\gamma}^\top(\Psi_l^{\mathrm{c}}) + \mathbf{Z} \in \mathbb{C}^{U(\Psi)\times U(\Psi^{\mathrm{c}})},\end{aligned} \tag{54}$$

where $\mathbf{Z}$ is the unfolded form of $\boldsymbol{\mathcal{Z}}$. The steering vector $\boldsymbol{\gamma}$ and its corresponding length $U$ are defined as

$$\boldsymbol{\gamma}(\Psi) = \bigotimes_{\xi_i \in \Psi} \boldsymbol{\alpha}(\zeta_{\xi_i}, U_i), \quad U(\Psi) = \prod_{\xi_i \in \Psi} U_i, \tag{55}$$

where $i$ is in ascending order.

In (54), the MUF makes the $\Psi$-related components explicit in the steering vector $\boldsymbol{\gamma}(\Psi)$, while the $\Psi^{\mathrm{c}}$-related components remain implicit as snapshots in $\mathbf{F}$. In other words, $\mathbf{F}$ can be regarded as an observation with a Kronecker steering vector form $\boldsymbol{\gamma}(\Psi)$ and a number of snapshots $U(\Psi^{\mathrm{c}})$. This naturally fits the multi-snapshot observation form required by subspace-based algorithms [40]. Noted that although the structure of the observation has been altered, the number of targets is still assumed to be accurately estimated. Thus, using the multi-snapshot observation $\mathbf{F}$ or sampled covariance matrix $\mathbf{R}_{\mathrm{F}} = \mathbf{F}\mathbf{F}^{\mathrm{H}}$, one can estimate $\hat{\Psi}_l, l = 1, 2, \ldots, L$ by applying existing methods such as MUSIC [36], propagator method [30], or ESPRIT [41].

*2) Estimation of $\Psi^{\mathrm{c}}$ based on the estimated $\hat{\Psi}$:* The second step of the sequential framework involves estimating $\Psi^{\mathrm{c}}$ corresponding to each $\hat{\Psi}_l$. Notably, all estimated parameters for the same target are automatically matched. This is guaranteed by the following proposition and property:

**Proposition 2.** *Given $\boldsymbol{\mathcal{F}}$ and arbitrary $\Psi \subsetneq \Theta$, (45) can always be expressed as:*

$$\rho(\Theta) = \frac{1}{\left(\bar{\boldsymbol{\gamma}}(\Psi) \otimes \bar{\boldsymbol{\gamma}}(\Psi^{\mathrm{c}})\right)^{\mathrm{H}} \boldsymbol{\Xi} \left(\bar{\boldsymbol{\gamma}}(\Psi) \otimes \bar{\boldsymbol{\gamma}}(\Psi^{\mathrm{c}})\right)}, \tag{56}$$

*where*

$$\bar{\boldsymbol{\gamma}}(\Psi) = \bigotimes_{\xi_i \in \Psi} \boldsymbol{\alpha}(\zeta_{\xi_i}, \bar{U}_i), \tag{57}$$

$$\boldsymbol{\Xi} = \hat{\mathbf{Q}}(\hat{\mathbf{Q}}^{\mathrm{H}}\hat{\mathbf{Q}})^{-1}\hat{\mathbf{Q}}^{\mathrm{H}}. \tag{58}$$

*Proof.* Note that (11) can be expressed as

$$\mathrm{vec}(\boldsymbol{\mathcal{F}}) = \sum_{l=1}^{L} \beta_l \boldsymbol{\gamma}(\Theta_l) + \mathrm{vec}(\boldsymbol{\mathcal{Z}}). \tag{59}$$

The product order within the Kronecker structure of $\boldsymbol{\gamma}$, i.e., $i$ is in ascending order, depends on the vectorization order of $\boldsymbol{\mathcal{F}}$. Thus, by rearranging the vectorization order in the order of $\Psi$ followed by $\Psi^{\mathrm{c}}$, denoted as $\mathrm{vec}_{\mathrm{re}}$, we get

$$\mathrm{vec}_{\mathrm{re}}(\boldsymbol{\mathcal{F}}) = \sum_{l=1}^{L} \beta_l \boldsymbol{\gamma}(\Psi_l) \otimes \boldsymbol{\gamma}(\Psi_l^{\mathrm{c}}) + \mathrm{vec}_{\mathrm{re}}(\boldsymbol{\mathcal{Z}}). \tag{60}$$

Then, by replacing the $\mathrm{vec}(\cdot)$ operator in (16) with $\mathrm{vec}_{\mathrm{re}}(\cdot)$ and updating (28), a new $\hat{\mathbf{Q}}$ and $\rho(\Theta)$ can be constructed (refer to Algorithm 1). Note that the formation of $\hat{\mathbf{Q}}$ depends on the vectorization order defined by $\Psi$. Moreover, smoothing modifies only the length of the steering vector while preserving its Kronecker structure [34]. As a result, after smoothing in the second step of Algorithm 1, the steering vector in (60) transforms into $\bar{\boldsymbol{\gamma}}(\Psi) \otimes \bar{\boldsymbol{\gamma}}(\Psi^{\mathrm{c}})$. By substituting $\bar{\boldsymbol{\alpha}}$ in (45) with $\bar{\boldsymbol{\gamma}}(\Psi) \otimes \bar{\boldsymbol{\gamma}}(\Psi^{\mathrm{c}})$, (56) is obtained, completing the proof. □

**Property 1.** *By applying the mixed-product property of the Kronecker product:*

$$(\mathbf{A} \otimes \mathbf{B})(\mathbf{C} \otimes \mathbf{D}) = (\mathbf{AC}) \otimes (\mathbf{BD}), \tag{61}$$

*it follows that for any $\boldsymbol{\alpha} \in \mathbb{C}^n$ and $\boldsymbol{\beta} \in \mathbb{C}^m$, we obtain:*

$$\boldsymbol{\alpha} \otimes \boldsymbol{\beta} = (\boldsymbol{\alpha} \otimes \mathbf{I}_m)(\mathbf{I}_1 \otimes \boldsymbol{\beta}) = (\boldsymbol{\alpha} \otimes \mathbf{I}_m)\boldsymbol{\beta} \tag{62}$$

*where $\mathbf{I}_m$ is the $m \times m$ identity matrix.*

Since the targets have already been distinguished in the $\Psi$ domain in the first step, only the estimation of each $\Psi_l^{\mathrm{c}}$ corresponding to the respective $\hat{\Psi}_l$ is required. For simplicity, we consider the reciprocal of (56). Based on Property 1, the cost function can then be expressed as

$$\begin{aligned} \frac{1}{\rho(\Theta)} &= \left(\bar{\boldsymbol{\gamma}}(\Psi) \otimes \bar{\boldsymbol{\gamma}}(\Psi^{\mathrm{c}})\right)^{\mathrm{H}} \boldsymbol{\Xi} \left(\bar{\boldsymbol{\gamma}}(\Psi) \otimes \bar{\boldsymbol{\gamma}}(\Psi^{\mathrm{c}})\right) \\ &= \bar{\boldsymbol{\gamma}}^{\mathrm{H}}(\Psi^{\mathrm{c}}) \left( (\bar{\boldsymbol{\gamma}}(\Psi) \otimes \mathbf{I}_{\bar{U}(\Psi^{c})} \right)^{\mathrm{H}} \boldsymbol{\Xi} \left( (\bar{\boldsymbol{\gamma}}(\Psi) \otimes \mathbf{I}_{\bar{U}(\Psi^{c})} \right) \bar{\boldsymbol{\gamma}}(\Psi^{\mathrm{c}}) \\ &= \bar{\boldsymbol{\gamma}}^{\mathrm{H}}(\Psi^{\mathrm{c}}) \tilde{\boldsymbol{\Xi}}(\Psi) \bar{\boldsymbol{\gamma}}(\Psi^{\mathrm{c}}), \end{aligned} \tag{63}$$

where

$$\tilde{\boldsymbol{\Xi}}(\Psi) = \left( (\bar{\boldsymbol{\gamma}}(\Psi) \otimes \mathbf{I}_{\bar{U}(\Psi^{c})} \right)^{\mathrm{H}} \boldsymbol{\Xi} \left( (\bar{\boldsymbol{\gamma}}(\Psi) \otimes \mathbf{I}_{\bar{U}(\Psi^{c})} \right), \tag{64}$$

and the corresponding steering vector length $\bar{U}$ is denoted by

$$\bar{U}(\Psi) = \prod_{\xi_i \in \Psi} \bar{U}_i. \tag{65}$$

By substituting the $L$ sets of estimated $\hat{\Psi}_l$ into (64), $L$ cost functions based on (63) are obtained, given by

$$\mu_l(\Psi^{\mathrm{c}}) = \bar{\boldsymbol{\gamma}}^{\mathrm{H}}(\Psi^{\mathrm{c}}) \tilde{\boldsymbol{\Xi}}(\hat{\Psi}_l) \bar{\boldsymbol{\gamma}}(\Psi^{\mathrm{c}}), \quad l = 1, 2, \ldots, L. \tag{66}$$

By minimizing the cost functions in (66), each $\hat{\Psi}_l^{\mathrm{c}}$ corresponding to $\hat{\Psi}_l$ is obtained, thereby completing the estimation.

Compared with (45), the proposed sequential framework reduces computational complexity by decomposing the multi-dimensional search into stage-wise estimations. However, this strategy may incur a certain accuracy loss. First, estimation errors in earlier stages can propagate to subsequent stages, especially under low-SNR conditions. Second, since part of the multi-dimensional structure is fixed after each stage, the effective exploitable degrees of freedom are reduced. Therefore, the framework represents a structured complexity-reduction trade-off.

**Remark 2.** *For multi-snapshot observations $\mathbf{F}$ in (54), the correlation between snapshots will be disrupted by $\boldsymbol{\gamma}(\Psi_l^{\mathrm{c}})$, thus smoothing is not strictly necessary. However, applying 1D/2D smoothing to each column of $\mathbf{F}$ can still improve the decorrelation performance of the smoothed observation. For further details, see [32] and [34].*

**Remark 3.** *The orthogonal spectrum dimensionality-reduction method based on Property 1 has been widely adopted [42]. Its main idea is to compress the search dimension by constructing and inverting a projection matrix at each grid point (e.g., (64)), where a lower-dimensional spectrum is first formed and the remaining parameters are recovered via least-squares estimation. Such approaches reduce computational burden and preserve parameter matching, but the final performance may depend on projection accuracy and the numerical stability of the least-squares step.*

*In contrast, the proposed method forms a multi-stage sequential estimation framework. Dimensionality reduction is achieved through structural factorization of the multi-dimensional harmonic model, where the super-resolution esti-*

*mate obtained at each stage is used as a conditional input for the next. While similarly reducing overall search complexity and maintaining parameter matching, the proposed framework preserves the super-resolution property of the spectral estimator at every stage.*

**Remark 4.** *The proposed sequential framework admits natural extension to higher-dimensional scenarios (e.g., MIMO-OFDM or azimuth-elevation arrays) by redefining parameter subsets and updating the corresponding partitions. Moreover, when $\Psi^{\mathrm{c}}$ contains multiple elements, it can be regarded as a new $\Theta$, enabling nested sequential estimation for further complexity reduction.*

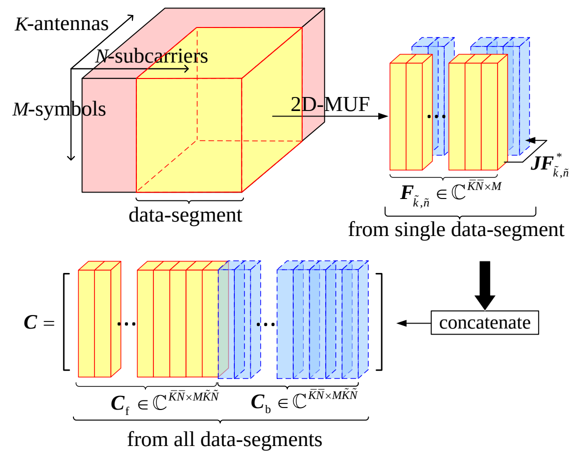


Fig. 6. Data smoothing in azimuth-range domain.

### B. An Implementation of Sequential Estimation Approach

In this subsection, we present a propagator-based sequential azimuth-range before Doppler (PS-AR-D) estimation method as an alternative to the PJ-ARD estimator, using the sequential framework in an ISAC scenario.

In the sequential framework, each unique $\hat{\Psi}_l$ is paired with a corresponding $\hat{\Psi}_l^{\mathrm{c}}$, with the parameters that are more difficult to distinguish across targets preferably assigned to $\Psi^{\mathrm{c}}$. For instance, when the angular resolution of radar is low, setting $\Psi = \{\tau, f_{\mathrm{D}}\}$ and $\Psi^{\mathrm{c}} = \{\theta\}$ allows for initial separation in the range-Doppler domain, followed by angle estimation to improve resolution. In ISAC, where OFDM symbols are transmitted in resource blocks, the limited number of symbols within a CPI may reduce Doppler resolution [43] [44]. Therefore, a more suitable setting is $\Psi = \{\theta, \tau\}$ and $\Psi^{\mathrm{c}} = \{f_{\mathrm{D}}\}$. The implementation steps are detailed below:

*1) Azimuth-Range Estimation through 2D-MUF:* Given the limited number of snapshots (or symbols), MUF is combined with 2D smoothing along the azimuth-range domain to enhance performance. According to $\Psi = \{\theta, \tau\}$, the forward smoothing window and the total number of forward observations, referred to as the data segment, are $\bar{K} \times \bar{N} \times M$ and $\tilde{K} \times \tilde{N}$, respectively. The 2D-MUF is first applied to each data segment of $\boldsymbol{\mathcal{F}}$ as

$$\begin{aligned}\mathbf{F}_{\tilde{k},\tilde{n}} &= \mathrm{MUF}\left(\boldsymbol{\mathcal{F}}[\tilde{k}:\tilde{k}+\bar{K}-1, \tilde{n}:\tilde{n}+\bar{N}-1, :], \{\theta,\tau\}\right)\\ &= \sum_{l=1}^{L} \zeta_{\theta_l}^{\tilde{k}} \zeta_{\tau_l}^{\tilde{n}} \beta_l \bar{\boldsymbol{\gamma}}(\{\theta,\tau\}) \boldsymbol{\gamma}^{\top}(\{f_{\mathrm{D}}\}) + \mathbf{Z}_{\tilde{k},\tilde{n}},\end{aligned} \tag{67}$$

where $\tilde{k}$ and $\tilde{n}$ are indices of the observations, defined in the same way as (12), $\mathbf{Z}_{\tilde{k},\tilde{n}}$ is a smoothed and unfolded version of additive noise $\boldsymbol{\mathcal{Z}}$. When $\tilde{k} = \tilde{n} = 1$, (67) is equivalent to (50). By sorting and concatenating all $\mathbf{F}_{\tilde{k},\tilde{n}}$ column-wise for each symbol, a forward smoothing observation is constructed as

$$\begin{aligned}\mathbf{C}_{\mathrm{f}} &= [\mathbf{F}_{0,0}, \mathbf{F}_{0,1}, \cdots, \mathbf{F}_{\tilde{k},\tilde{n}}, \cdots, \mathbf{F}_{K-1,N-1}]\\ &= \bar{\boldsymbol{\Gamma}}_1 \mathbf{B} (\tilde{\boldsymbol{\Gamma}}_1 \odot \boldsymbol{\Gamma}_2)^{\top} + \mathbf{Z}_{\mathrm{c}},\end{aligned} \tag{68}$$

where

$$\bar{\boldsymbol{\Gamma}}_1 = [\bar{\boldsymbol{\gamma}}(\{\theta_1,\tau_1\}), \bar{\boldsymbol{\gamma}}(\{\theta_2,\tau_2\}), \cdots, \bar{\boldsymbol{\gamma}}(\{\theta_L,\tau_L\})], \tag{69}$$

$$\tilde{\boldsymbol{\Gamma}}_1 = [\tilde{\boldsymbol{\gamma}}(\{\theta_1,\tau_1\}), \tilde{\boldsymbol{\gamma}}(\{\theta_2,\tau_2\}), \cdots, \tilde{\boldsymbol{\gamma}}(\{\theta_L,\tau_L\})], \tag{70}$$

$$\boldsymbol{\Gamma}_2 = [\boldsymbol{\gamma}(\{f_{\mathrm{D}1}\}), \boldsymbol{\gamma}(\{f_{\mathrm{D}2}\}), \cdots, \boldsymbol{\gamma}(\{f_{\mathrm{D}L}\})], \tag{71}$$

$$\mathbf{Z}_{\mathrm{c}} = [\mathbf{Z}_{0,0}, \mathbf{Z}_{0,1}, \cdots, \mathbf{Z}_{\tilde{k},\tilde{n}}, \cdots, \mathbf{Z}_{K-1,N-1}], \tag{72}$$

and

$$\tilde{\boldsymbol{\gamma}}(\{\theta_l,\tau_l\}) = \boldsymbol{\alpha}(\zeta_{\theta_l}, \tilde{K}) \otimes \boldsymbol{\alpha}(\zeta_{\tau_l}, \tilde{N}). \tag{73}$$

The data smoothing in the azimuth-range domain is illustrated in Fig. 6. As the focus is on angle and range parameters, forward-backward smoothing and the extended propagator can be used for parameter estimation. Define a structured index space

$$\tilde{\mathcal{I}} = \left\{\boldsymbol{i} = (u_1,u_2) \,\middle|\, 1 \le u_d \le \bar{U}_d,\ d = 1,2\right\}, \tag{74}$$

and define a bijective mapping as

$$\tilde{\kappa}(u_1,u_2) = (u_1-1)\bar{U}_2 + u_2. \tag{75}$$

The complete smoothed observation matrix is then constructed and partitioned as

$$\mathbf{C} = [\mathbf{C}_{\mathrm{f}}, \mathbf{C}_{\mathrm{b}}], \tag{76}$$

$$\mathbf{C}_1 = \mathbf{C}[\tilde{\kappa}(\tilde{\mathcal{S}}), :], \tag{77}$$

$$\mathbf{C}_2 = \mathbf{C}[\tilde{\kappa}(\tilde{\mathcal{I}} \setminus \tilde{\mathcal{S}}), :], \tag{78}$$

where $\mathbf{C}_{\mathrm{b}} = \mathbf{J}_{\bar{K}\bar{N}} \mathbf{C}_{\mathrm{f}}^{*}$, and $|\tilde{\mathcal{S}}| = L$ is a subset of $\tilde{\mathcal{I}}$ such that

$$\exists\ \boldsymbol{i}_1, \boldsymbol{i}_2, \boldsymbol{i}_3 \in \tilde{\mathcal{S}},\ (\boldsymbol{i}_2 - \boldsymbol{i}_1) \times (\boldsymbol{i}_3 - \boldsymbol{i}_1) \ne \mathbf{0}. \tag{79}$$

Following the extended propagator method, we locate the $L$ peaks in the spectrum

$$\tilde{\rho}(\theta,\tau) = \frac{1}{\bar{\boldsymbol{\gamma}}^{\mathrm{H}}(\{\theta,\tau\}) \hat{\mathbf{Q}}_{\mathrm{c}} (\hat{\mathbf{Q}}_{\mathrm{c}}^{\mathrm{H}} \hat{\mathbf{Q}}_{\mathrm{c}})^{-1} \hat{\mathbf{Q}}_{\mathrm{c}}^{\mathrm{H}} \bar{\boldsymbol{\gamma}}(\{\theta,\tau\})}, \tag{80}$$

where

$$\hat{\mathbf{Q}}_{\mathrm{c}} = \tilde{\mathbf{\Pi}}[\hat{\mathbf{P}}_{\mathrm{c}}^{\top}, -\mathbf{I}_{\bar{K}\bar{N}-L}]^{\top}, \tag{81}$$

$$\hat{\mathbf{P}}_{\mathrm{c}} = \left(\mathbf{C}_1\mathbf{C}_1^{\mathrm{H}}\right)^{-1}\mathbf{C}_1\mathbf{C}_2^{\mathrm{H}}, \tag{82}$$

$$\mathbf{\Pi} = \begin{bmatrix} \mathbf{I}_{\bar{K}\bar{N}}[\tilde{\kappa}(\tilde{\mathcal{S}}),:] \\ \mathbf{I}_{\bar{K}\bar{N}}[\tilde{\kappa}(\tilde{\mathcal{I}}\setminus\tilde{\mathcal{S}}),:] \end{bmatrix}. \tag{83}$$

Then, the paired estimation of $\hat{\theta}_l$ and $\hat{r}_l$ can be obtained corresponding to peak coordinates. Note that $(\hat{\mathbf{Q}}_{\mathrm{c}}^{\mathrm{H}}\hat{\mathbf{Q}}_{\mathrm{c}})^{-1}$ can be also efficiently computed like (46).

*2) Doppler Estimation Based on Estimated Azimuth-Range:* With $\hat{\theta}_l$ and $\hat{r}_l$ estimated for $l = 1, 2, \cdots, L$, $\Psi^{\mathrm{c}} = \{f_{\mathrm{D}}\}$ is subsequently determined. Given that the Kronecker structure of $\bar{\boldsymbol{\alpha}}$ aligns with the format in (60), $\tilde{\mathbf{Q}}(\Psi)$ is set to $\hat{\mathbf{Q}}$. Consequently, according to (66), the following expression is obtained:

$$\mu_l(f_{\mathrm{D}}) = \bar{\boldsymbol{\gamma}}^{\mathrm{H}}(\{f_{\mathrm{D}}\})\tilde{\mathbf{\Xi}}(\{\hat{\theta}_l, \hat{\tau}_l\})\bar{\boldsymbol{\gamma}}(\{f_{\mathrm{D}}\}). \tag{84}$$

Since $\bar{\boldsymbol{\gamma}}(f_{\mathrm{D}}) = \boldsymbol{\alpha}(\zeta_{f_{\mathrm{D}}}, \bar{M})$, (84) becomes a phase rotation estimation problem for $\zeta_{f_{\mathrm{D}}}$. This can be solved using the root method without parameter search similar to the root-MUSIC method [45] [46], as the root-based formulation of the propagator is essentially a Pisarenko harmonic decomposition [37]. Let $z = \zeta_{f_{\mathrm{D}}}$, and since $z^* = z^{-1}$, (84) is equivalently expressed as a polynomial equation as

$$p_l(z) = z^{\bar{M}-1}\boldsymbol{\alpha}^{\top}(z^{-1}, \bar{M})\tilde{\mathbf{\Xi}}(\{\hat{\theta}_l, \hat{\tau}_l\})\boldsymbol{\alpha}(z, \bar{M}) = 0. \tag{85}$$

As the roots corresponding to the Doppler frequency lie on the unit circle, the root $\hat{z}$ closest to the unit circle in the z-plane is identified from (85), and $v_l$ is then determined from its phase.

$$\hat{v}_l = \frac{c \cdot \arg(\hat{z})}{4\pi T_s f_c}. \tag{86}$$

A joint azimuth-range-Doppler estimation for multiple targets is now achieved. The implementation of the PS-AR-D estimator is summarized in Algorithm 2.

**Remark 5.** *When some targets cannot be well resolved in the first-stage azimuth-range domain, multiple roots close to the unit circle may appear during the Doppler estimation. Based on the correspondence between roots and spectral peaks [46], to improve reliability, one can further validate these roots by cross-checking with estimated azimuth-range and examining the corresponding local region in the 3D spectrum (45). A root is considered likely to correspond to a true target only if its mapped parameters coincide with a prominent spectral peak.*

**Remark 6.** *In the considered model (10), parameters across different dimensions are decoupled, enabling an arbitrary estimation order. The proposed method can thus be extended to general multi-dimensional harmonic decomposition problems, provided that not all parameters are fully coupled, without assuming a Kronecker structure. Whenever certain parameter groups can be separated from the vectorized formulation such as (59), a feasible estimation order exists for deploying the sequential framework. For instance, it can be applied in FMCW radar systems [47] for range-Doppler estimation prior to angle estimation, or in massive MIMO systems [48] for spatial channel estimation followed by delay-domain estimation.*

**Algorithm 2:** The Proposed PS-AR-D Estimator with Super-Resolution

**Input:** $\boldsymbol{\mathcal{F}} \in \mathbb{C}^{K\times N\times M}, \bar{K}, \bar{M}, \bar{N}, \Delta f, T_{\mathrm{s}}, \lambda, c, f_c, d.$

Perform azimuth-range smoothing on $\boldsymbol{\mathcal{F}}$, then apply 2D-MUF to each data segment as in (67).
Construct $\mathbf{C}_{\mathrm{f}}$ and $\mathbf{C}$ using (68) and (76).
Estimate $L$ using methods from [38] or [39], and determine the set $\tilde{\mathcal{S}}$ that satisfies condition (79).
Compute the corresponding mapped indices according to (28) and (75).
Partition $\mathbf{C}$ as in (77)(78), and compute $\hat{\boldsymbol{P}}_{\mathrm{c}}$ and $\hat{\boldsymbol{Q}}_{\mathrm{c}}$ using (82) and (81).
Calculate (80) based on the parameter grid, find the $L$ largest peaks, and estimate azimuth $\hat{\theta}_l$ and range $\hat{r}_l$, for $l = 1, 2, \ldots, L$.
Compute $\hat{\boldsymbol{Q}}$ following Algorithm 1.
Construct $\tilde{\mathbf{\Xi}}(\{\hat{\theta}_l, \hat{\tau}_l\})$ using (64), where $\hat{\tau}_l = 2\hat{r}_l/c$.
Construct $p_l$ using (85) and find the root closest to the unit circle; calculate the corresponding $\hat{v}_l$ from (86).

**Output:** $\hat{\theta}_l, \hat{r}_l, \hat{v}_l$.

### C. Discussion of Complexity

We discuss the impact of the sequential framework on computational complexity. The major computational complexity of the PJ-ARD estimator is given by $\mathscr{C}_{\mathrm{PJ-ARD}} = \mathcal{O}[\bar{W}^2 + L\bar{W}\tilde{W} + L\left(\bar{W} - L\right)^2 + \Delta\left(\Theta\right)\bar{W}^2]$, where $\Delta(\Theta)$ represents the number of grid points corresponding to the partitioning of all parameters in $\Theta$. Since $\bar{W} = \bar{K}\bar{N}\bar{M}$ and $\Theta = \{\theta, \tau, f_{\mathrm{D}}\}$, the computational complexity of the last term $\Delta(\Theta)\bar{W}^2$ in the PJ-ARD estimator grows exponentially with the increase in data size and grid size.

In contrast, the sequential framework divides the parameter set $\Theta$ into $\Psi$ and $\Psi^{\mathrm{c}}$, and constructs distinct $\mu_l$ to ensure that each $\Psi^{\mathrm{c}}$ aligns with the estimated $\hat{\Psi}$. The computational complexity for calculating all cost functions is $\mathcal{O}[\Delta(\Psi)U^2(\Psi) + L\Delta(\Psi^{\mathrm{c}})U^2(\Psi^{\mathrm{c}})]$. Noting that $\Delta(\Theta) = \Delta(\Psi) \cdot \Delta(\Psi^{\mathrm{c}})$, the complexity of calculating the cost function is significantly lower than that of the PJ-ARD estimator.

As an example, in the PS-AR-D estimator, the forward-backward smoothed observation $\mathbf{C}$ is first constructed, and an orthonormal propagator is used to form the noise subspace for azimuth-range estimation in (80). The computational complexity for this step is $\mathscr{C}_1 = \mathcal{O}[\bar{K}^2\bar{N}^2M + L\bar{K}\bar{N}\tilde{K}\tilde{N} + L(\bar{K}\bar{N} - L)^2 + \Delta(\{\theta, \tau\})(\bar{K}\bar{N})^2]$. Next, by substituting the estimated azimuth-range, the corresponding Doppler for each target is estimated through a polynomial equation (85). The computational complexity of this step is $\mathscr{C}_2 = \mathcal{O}[\bar{W}^2 + L\bar{W}\tilde{W} + L(\bar{W} - L)^2 + L\bar{W}^2\bar{M} + L\bar{M}^3 + L^2\bar{M}^2 + L^3\bar{M}]$. When $\bar{K}$, $\bar{N}$, $\bar{M}$, $\tilde{K}$, $\tilde{N}$ and $\tilde{M}$ are of the same order, the ratio of the computational complexity of the PS-AR-D estimator to the PJ-ARD estimator is approximately given by

$$\frac{\mathscr{C}_1 + \mathscr{C}_2}{\mathscr{C}_{\mathrm{PJ-ARD}}} \approx \frac{\bar{M}L + \frac{\Delta(\{\theta,\tau\})}{\bar{M}^2}}{2L + \Delta\left(\{\theta, \tau, f_{\mathrm{D}}\}\right)}. \tag{87}$$

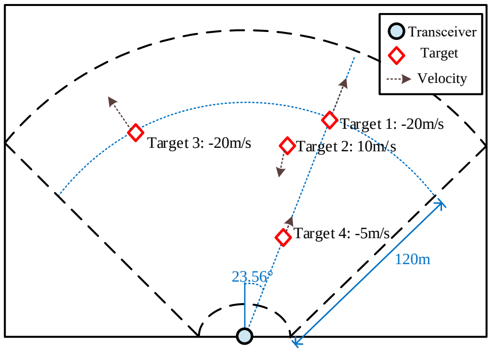


Fig. 7. Simulation scene: azimuth-range-velocity parameters of four targets to be estimated, some targets have the same azimuth, while some targets have the same velocity and range relative to the sensing antenna.

Although both complexities increase with $L$ and PS-AR-D grows faster, $L$ is typically much smaller than the grid size. Moreover, $\Delta(\{\theta,\tau\})/\bar{M}^2 \ll \Delta(\{\theta,\tau,f_{\rm D}\})$, so PS-AR-D generally has a lower computational burden. As the grid size increases, the advantages of PS-AR-D over PJ-ARD become more pronounced. A more detailed comparison can be found in the next section.

## V. Simulations

In this section, the effectiveness of the proposed methods is evaluated through numerical simulations. A multi-target scenario is considered, where four targets need to be localized. Some targets share the same angular parameters, while others have identical radial range and velocity relative to the sensing antennas. The midpoint of the antenna array is used as the reference point. As shown in Fig. 7, the targets are positioned at $(23.56°, 120\text{m})$, $(13.98°, 100\text{m})$, $(-30°, 120\text{m})$, and $(23.56°, 50\text{m})$, with corresponding radial velocities of $-20\text{m/s}$, $10\text{m/s}$, $-20\text{m/s}$, and $-5\text{m/s}$, respectively. Additionally, the reflectivity factors of the targets are set to 0.1, 0.04, 0.06, and 0.09, respectively. Without loss of generality, the noise is assumed to be additive white Gaussian noise. At the transmitter, a relatively small bandwidth and pulse duration were selected to evaluate the super-resolution capability. Specifically, a subcarrier spacing of $\Delta f = 90$ kHz and a carrier frequency of $f_c = 24$ GHz, with a CPI consisting of 24 modulated OFDM symbols, each containing 32 subcarriers. This configuration also demonstrates the flexibility of the proposed algorithm across different protocols and hardware platforms. Under this configuration, the total bandwidth is $B = N\Delta f = 2.88\,\text{MHz}$, yielding a range resolution of $\Delta R = c/(2B) \approx 52.08\,\text{m}$. The period of a single OFDM symbol is $T_{\rm s} = T_{\rm d} + T_{\rm cp} = 13.89\,\mu\text{s}$, where $T_{\rm cp} = (1/4)T_{\rm d}$. The velocity resolution, limited by the CPI of $M$ symbols, is given by $\Delta v = c/(2f_c M T_{\rm s}) \approx 28.12\,\text{m/s}$. The smoothing coefficients are fixed at $\bar{N}/N = \bar{M}/M = 1/2$, as in [23]. At the receiver, a standard ULA antenna configuration is employed. The number of equivalent array antennas, $K$, is set to 8, and the length of the smoothing window, $\bar{K}$, is fixed at 6.

### A. Super-Resolution Estimation in Multi-Target Scene

First, the high-dimensional super-resolution performance of the proposed methods is examined and compared with 2D-DFT [13] and 2D-MUSIC [23] [32] combined with DBF. In this analysis, the SNR at the receiver is assumed to be 15 dB.

In range and Doppler estimation, as illustrated in Fig. 8(a), the conventional 2D-DFT method demonstrates limited performance. This limitation primarily stems from its inherent requirement for larger signal bandwidth and extended CPI to attain high resolution. In contrast, Figs. 8(b)-(e) present the estimation results obtained through super-resolution techniques, where clearly defined peaks in the spectrum are evident. Notably, the 2D-MUSIC algorithm generates two distinct peaks along with a weaker one, which indicates its failure to differentiate and match all four targets. In comparison, the PJ-ARD estimator effectively distinguishes all four targets and precisely estimates their range-Doppler parameters as shown in Figs. 8(c)-(e). In view of the complexity involved in visualizing 3D spectra, the estimation performance of the PJ-ARD estimator is presented using range-velocity profiles (RV-Ps) at selected angles. The azimuth estimation is shown in Fig. 9. The DBF not only exhibits deviation in estimating the spectrum peak but also causes the main lobes to overlap. Using the PJ-ARD estimator, azimuths are distinctly separated within the range-Doppler domain. Each target is associated with its own azimuth profile (A-P), and can be estimated from the spectrum correctly.

The range-angle spectrum of the PS-AR-D estimator under the identical scenario is depicted in Fig. 10. The results demonstrate that the PS-AR-D preserves a target resolution capability comparable to that of the PJ-ARD estimator, with each target exhibiting distinct separability. However, intrinsic to its design, the PS-AR-D algorithm does not generate Doppler spectrum outputs. A evaluation of its Doppler estimation performance will be analyzed in the subsequent subsection. Note that for the proposed methods, while the simulation results are presented in separate dimensions, the parameter estimates are inherently matched across all dimensions for each target.

### B. Estimation Accuracy

For accuracy analysis, the proposed method is evaluated under the same scenario depicted in Fig. 7. Without loss of generality, the root mean square errors (RMSEs) of parameter estimation for all targets are analyzed across multiple established methods: DBF, 1D-MUSIC [17] for azimuth estimation, 2D-DFT [14], 2D-MUSIC [23] for range-Doppler estimation, 3D-MUSIC [25], 3D-ESPRIT [26], and the proposed algorithms. The performance comparison is based on the average RMSE values, defined as:

$$\text{RMSE} = \frac{1}{L}\sum_{l=1}^{L}\sqrt{\frac{1}{N_{\rm m}}\sum\nolimits_{i=1}^{N_{\rm m}}[(\hat{\xi}_{i,l}-\xi_{i,l})^2]}, \tag{88}$$

where $N_{\rm m} = 300$ represents the number of Monte Carlo simulations conducted, $\hat{\xi}_{i,l}$ and $\xi_{i,l}$ denote the estimated and actual parameter values for target $l$ in the $i$-th simulation, respectively. The low dimensional methods exhibit obvious limitations: DBF and 1D-MUSIC demonstrate inadequate

(a) 2D-FFT

(b) 2D-MUSIC

(c) RV-P 1 of PJ-ARD

(d) RV-P 2 of PJ-ARD

(e) RV-P 3 of PJ-ARD

Fig. 8. Comparison of the joint range-velocity estimation at SNR=15 dB, with 32 subcarriers and 24 OFDM symbols, (a) 2D-DFT; (b) 2D-MUSIC; (c)-(e) PJ-ARD, the graphs in (c)-(e) show spectrum profiles at azimuths of 23.56°(RV-P 1), 13.98°(RV-P 2), and -30°(RV-P 3), respectively.

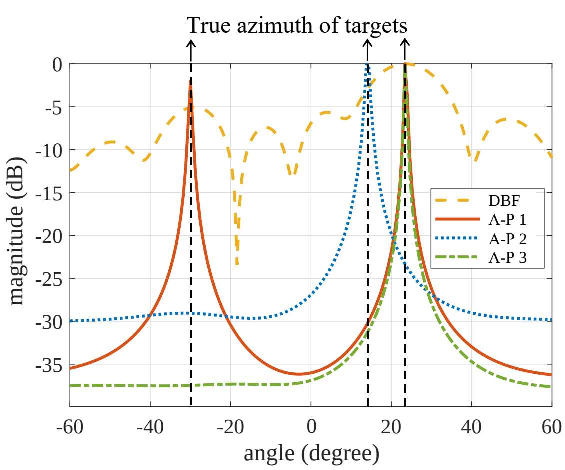


Fig. 9. Comparison of the azimuth estimation at SNR=15 dB, using a ULA with 8 elements. The AP 1 to 3 of PJ-ARD show spectrum profiles at range-velocity of (120$m$, -20$m/s$), (100$m$, 10$m/s$), and (50$m$, –5$m/s$) respectively.

Fig. 10. Azimuth and range estimations for the PS-AR-D estimator, using a ULA with 8 elements and 32 subcarriers of each OFDM symbols.

performance in resolving azimuth-overlapping targets, while 2D-DFT and 2D-MUSIC exhibit constrained capability in separating range-Doppler overlapping targets. Despite these inherent limitations, their performance metrics remain analyzable within respective operational dimensions. The square-root Cramér-Rao Bound (RCRB) is also incorporated in the simulations, with detailed derivations available in [26] and [49].

Figs. 11-13 illustrate the RMSEs of azimuth, range, and velocity estimates versus SNR for the considered algorithms. The overall trends are consistent across all three parameters. At low-SNR, 3D-MUSIC achieves the best accuracy. As SNR increases, PJ-ARD improves and becomes competitive with 3D-MUSIC. PS-AR-D also exhibits a clear reduction in RMSE as SNR increases, outperforming 1D-MUSIC, 2D-MUSIC, and 3D-ESPRIT; however, its accuracy remains slightly below that of PJ-ARD, particularly in the low-SNR regime. By contrast, DBF and 2D-DFT are constrained by aperture and bandwidth limitations, resulting in persistently high RMSEs across all SNR values. Finally, while PJ-ARD achieves higher estimation accuracy than PS-AR-D at moderate-to-high SNR, the latter offers substantially lower computational complexity, as will be discussed in Section V-D.

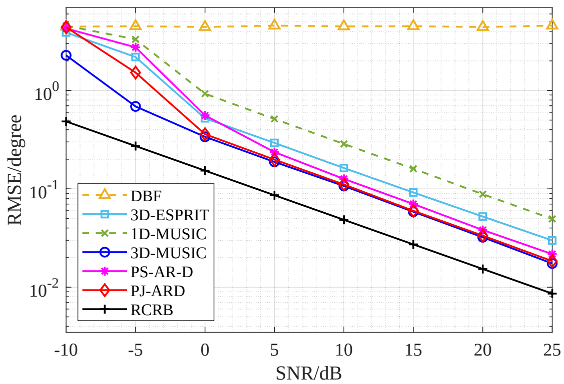


Fig. 11. Comparison of the RMSEs of estimated azimuths.

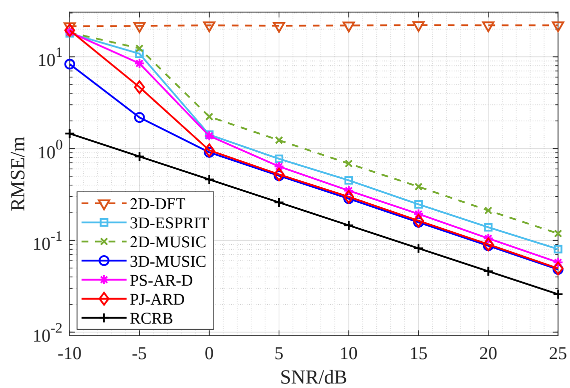


Fig. 12. Comparison of the RMSEs of estimated ranges.

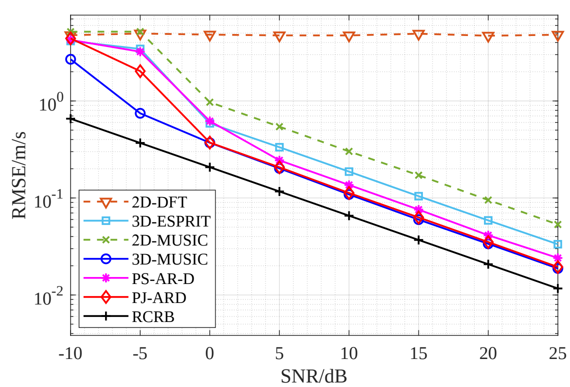


Fig. 13. Comparison of the RMSEs of estimated velocities.

## C. Performance Evaluation under Model Order Mismatch

In this subsection, the performance of the considered algorithms is evaluated under model order mismatch conditions. A detection is deemed successful if the coordinate differences between the largest $L$ estimated peaks and the corresponding true parameters are all within 20 times the RCRB. The SNR is fixed at 10 dB, and the target scenario is identical to that shown in Fig. 7.

Fig. 14 evaluates the detection performance and accuracy of the considered algorithms under different assumed model orders (i.e., preset target numbers) by plotting the true peak detection rate (TPDR) and normalized root mean square error

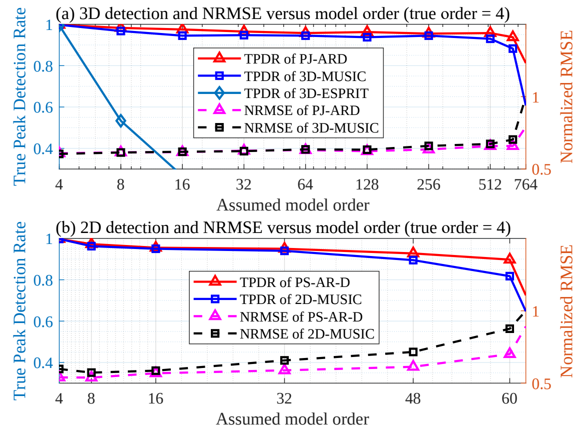


Fig. 14. Comparison of the TPDR and NRMSEs versus preset model order.

(NRMSE). The NRMSE is obtained by normalizing the RMSE and then averaging across all dimensions. This is reasonable because the RMSE trends along different dimensions are similar, as shown in the previous subsection.

In the 3D case (Fig. 14(a)), PJ-ARD and 3D-MUSIC maintain similarly high TPDR across a broad range of model order settings, while 3D-ESPRIT suffers sharp performance degradation due to its inability to effectively distinguish spurious results from true ones. PJ-ARD also keeps its NRMSE low and stable, showing better robustness than 3D-MUSIC under severe model mismatch. In the 2D case (Fig. 14(b)), PS-AR-D achieves higher detection and estimation accuracy than 2D-MUSIC, maintaining high TPDR and low NRMSE even when the assumed model order deviates from the true value.

## D. Computational Complexity and Runtime Analysis

This subsection presents both the quantitative evaluation of computational complexity and the measured runtime of the considered algorithms. Fig. 15 shows how the computational demand (FLOPs) varies with the number of sensors, subcarriers, and OFDM symbols. In particular, Fig. 15(a) compares complexities versus the number of sensors with $N = 64$ and $M = 24$; Fig. 15(b) versus the number of subcarriers with $K = 32$ and $M = 24$; and Fig. 15(c) versus the number of OFDM symbols with $K = 32$ and $N = 64$. The number of targets is set to $L = 4$, with $\bar{K}/K = \bar{N}/N = \bar{M}/M = 1/2$, and the azimuth-range and range-velocity search grids contain 500 and 1000 points, respectively.

It can be seen that the 3D-MUSIC estimator has the highest computational cost, whereas the PS-AR-D estimator reduces complexity by two to three orders of magnitude, thanks to the avoidance of eigenvalue decomposition and multi-dimensional spectral search. PJ-ARD falls in between: as the data size increase, it requires less computation than 3D-ESPRIT. Notably, the complexity of PS-AR-D remains nearly constant with the number of OFDM symbols, since the number of symbols primarily affects the matrix size in the second stage of the sequential framework, which is much smaller than that in the first stage.

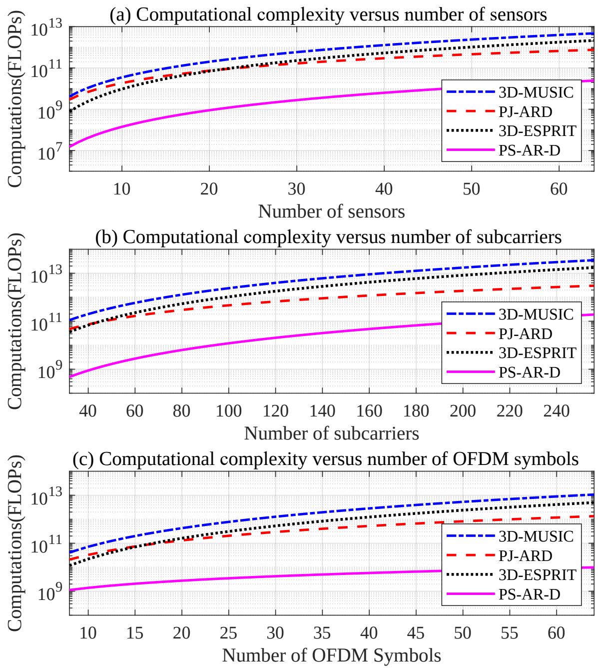


Fig. 15. Comparison of computational complexities in FLOPs versus (a) the number of sensors; (b) the number of subcarriers; (c) the number of OFDM symbols.

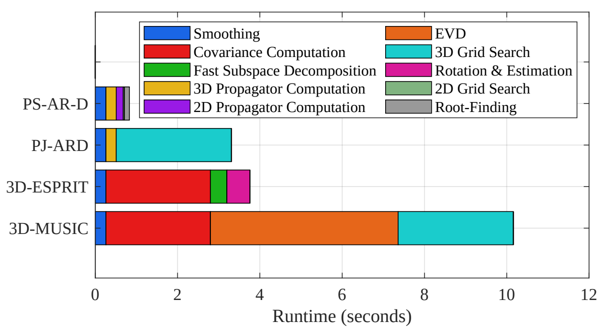


Fig. 16. Breakdown of computational time for each algorithm.

Under the same default parameter settings as in the complexity analysis, Fig. 16 provides a breakdown of the runtime for each algorithm. It can be observed that the proposed algorithms achieve significant runtime savings compared to 3D-MUSIC, particularly in the avoidance of covariance computation and EVD. 3D-ESPRIT alleviates the burden of grid search by replacing it with rotation and estimation steps, yet still incurs a non-negligible cost due to full covariance construction and subspace decomposition. In contrast, PS-AR-D further reduces computational load through parameter decoupling, eliminating the need for high-dimensional searches and making it the most time-efficient among the evaluated methods.

Importantly, although the grid search in the PJ-ARD estimator may pose a non-trivial computational burden, it can be controlled by adjusting the grid resolution. Therefore, this approach is more suitable for scenarios involving locally refined or small-size search grids. In scenarios with stringent real-time requirements, the use of a sequential framework such as PS-AR-D is recommended, as it notably reduces computational burden with only a minor loss in accuracy.

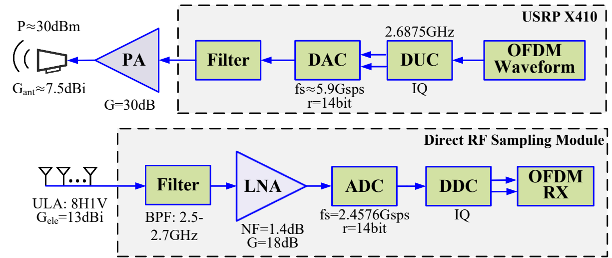


Fig. 17. The schematic of the experimental setup.

## VI. Experimental Measurements

In this section, we validate the proposed algorithms using a 2.6 GHz OFDM-based ISAC experimental system. The schematic and devices of the experimental setup are illustrated in Fig. 17 and Fig. 18(a), respectively. A commercial USRP X410 is used as the signal transmitter, connected to a power amplifier (PA) and a horn antenna. Specifically, after digital-to-analog conversion and filtering, a single-channel analog signal centered at 2.6875 GHz is generated. This signal is amplified and radiated via the horn antenna, with a total radiated power of approximately 30 dBm.

On the receiver side, a custom-designed direct RF sampling module is employed, connected to a vertically polarized 8-element ULA with inter-element spacing equal to half a wavelength at 2.6 GHz. The analog signals received by the ULA are directly sampled and digitally downconverted to baseband OFDM data, which are then processed by a computer for parameter estimation. The outdoor detection experiment is conducted using the deployed platform, as illustrated in Fig. 18(b). The targets are DJI Mavic 3E UAVs, and the OFDM waveform is transmitted via a horn antenna positioned 2 m from the receiver. Three UAVs operate within a radial range of 25–100 m and an azimuth sector of $-20^\circ$ to $20^\circ$, as illustrated in Fig. 18(c). The system employs 256 subcarriers with a 30 kHz spacing, yielding a baseband bandwidth of 7.68 MHz. Each frame spans 4.5 ms and contains 128 OFDM symbols. The corresponding range and velocity resolutions are approximately 19.53 m and 12.4 m/s, respectively.

Approximate ground-truth positions of UAVs 1, 2, and 3, as measured by a real-time kinematic (RTK) GPS system, are indicated by square, diamond, and triangle markers, respectively. As shown in Figs. 19(a)–19(b), the 2D-DFT method yields merged peaks for Targets 1 and 2, while the peak corresponding to Target 3 exhibits noticeable spreading in the range–Doppler domain. Figs. 19(c)–19(f) depict the RV-Ps and A-Ps extracted at the local maxima of the PJ-ARD 3D spectrum, where the peaks of multiple targets are distinctly separated. Figs. 19(g)–19(h) shows the spectrum obtained by the PS-AR-D method in the range–angle domain, along with the corresponding Doppler estimates for each spectral peak, in which all targets are clearly resolved. Note that although another peak appears in Fig. 19(e), it is not a local maximum

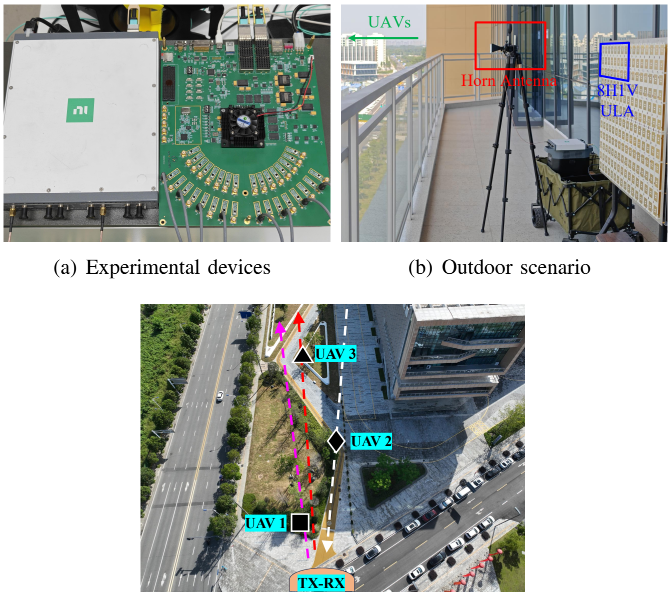


(a) Experimental devices (b) Outdoor scenario

(c) Flight route of UAVs

Fig. 18. Illustration of the experimental setup.

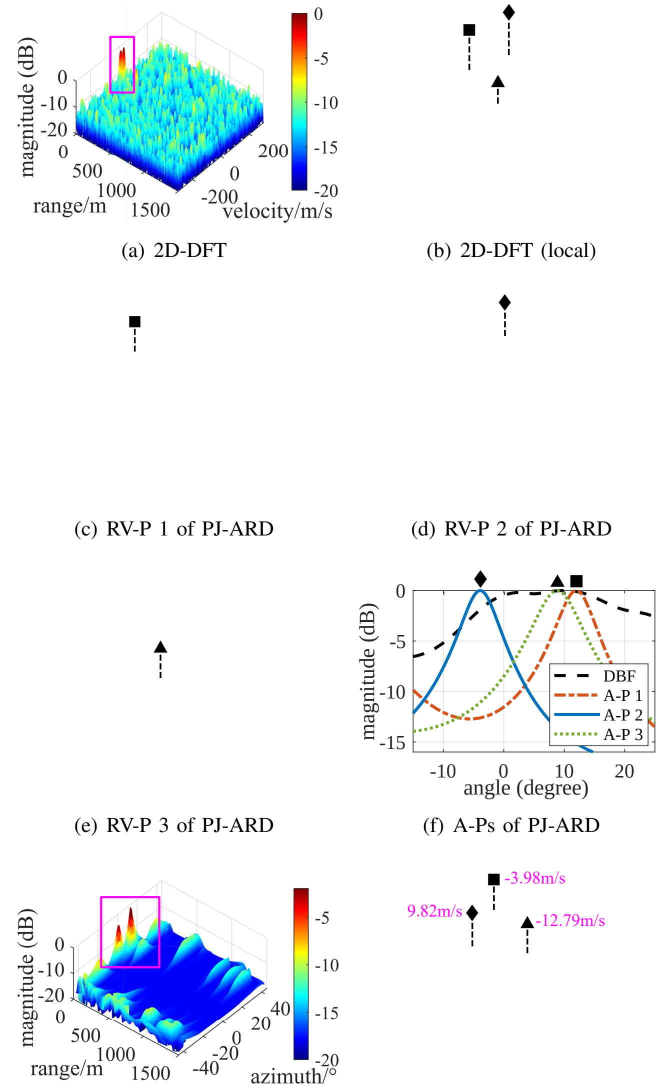


(a) 2D-DFT (b) 2D-DFT (local)

(c) RV-P 1 of PJ-ARD (d) RV-P 2 of PJ-ARD

(e) RV-P 3 of PJ-ARD (f) A-Ps of PJ-ARD

(g) PS-AR-D (h) PS-AR-D (Local)

Fig. 19. Comparison of 2D-DFT and the proposed methods for measured data. "Local" denotes a local display of the spectrum around the target region.

in the angle domain and is therefore not considered a valid estimation result. The 3D-MUSIC results are visually similar to PJ-ARD and are omitted for brevity. For a 10,000-point 3D grid, the covariance construction, EVD, and 3D search of 3D-MUSIC require 353.96 s, 1061.37 s, and 459.41 s, respectively, whereas the construction of the 3D and 2D propagators of the proposed method requires only 150.40 s and 20.97 s, greatly reducing computational time.

It is worth noting that, for clarity of presentation, only the local profiles containing the three peaks within the parameter ranges of the targets are shown. In practical implementation of the PJ-ARD and PS-AR-D methods, the model order is set to 64, which is much larger than the known number of targets. This choice is due to the presence of substantial interference and clutter in the measured data. Although direct-path suppression [50] and stationary-target removal [51] are applied as preprocessing steps, the model order cannot be accurately determined, and setting it equal to the known number of targets fails to yield reliable estimation results. Consequently, non-spectral methods such as ESPRIT have difficulty distinguishing true targets from the large number of spurious estimates in such scenarios. Recall the result in Section V-C.

## VII. Conclusions

This paper investigates joint azimuth-range-Doppler high-resolution target parameter estimation using OFDM waveforms. Leveraging the orthogonality of the subspaces, an extended propagator based on forward-backward smoothed observations is developed, referred to as the PJ-ARD method. To alleviate its computational burden caused by spectral search, a sequential framework is further proposed, which reduces search dimensionality and shortens steering vectors. Both simulations and experimental results demonstrate that the proposed approach achieves high-resolution joint parameter estimation with controllable computational complexity. In particular, the sequential method significantly reduces complexity with only a slight loss of accuracy. Both methods provide flexibility and scalability for higher-dimensional sensing applications. Future work will focus on adapting these approaches to practical scenarios by integrating them with existing communication protocols and multistatic base station systems.

## Appendix A
## Proof of Proposition 1

Recall from (13) that each steering vector is a Kronecker product of three Vandermonde vectors. Hence, the entry of $\bar{\mathbf{A}}$ indexed by a multi-index $(u_1, u_2, u_3)$ and target $l$ can be written as the monomial

$$\bar{\mathbf{A}}\left[\kappa(u_1, u_2, u_3),\, l\right] = \zeta_{\theta_l}^{u_1-1}\, \zeta_{\tau_l}^{u_2-1}\, \zeta_{f_{\mathrm{D}l}}^{u_3-1}, \quad 1 \leq u_d \leq \bar{U}_d. \tag{89}$$

Under a fixed Kronecker-consistent vectorization order, the row index increases first along the last dimension, then the second, then the first. Therefore, the first $\prod_{d=1}^{j} \bar{U}_d$ rows exhaust all combinations of indices in the first $j$ dimensions while fixing all indices in dimensions $d > j$ to their initial values. By the definition of $\delta(L)$ in (29), the index set of the first $L$ rows are contained in the first $\prod_{d=1}^{\delta(L)} \bar{U}_d$ rows of $\bar{\mathbf{A}}$, and thus all selected rows satisfy

$$u_d = 1, \quad \forall d > \delta(L). \tag{90}$$

Substituting (90) into (89) yields

$$\bar{\mathbf{A}}_1[s, l] = \prod_{d=1}^{\delta(L)} \zeta_{\xi_d, l}^{u_d(s)-1} \tag{91}$$

for every selected row, and is independent of $\{\zeta_{\xi_d,l}\}_{d>\delta(L)}$, where $(\xi_1, \xi_2, \xi_3) = (\theta, \tau, f_{\mathrm{D}})$ and $u_d(s)$ denotes the $d$-th index of the $s$-th selected row.

According to (91), the columns of $\bar{\mathbf{A}}_1$ are invariant to $\{\zeta_{\xi_d,l}\}_{d>\delta(L)}$. Hence, if two targets $l \neq l'$ share the same parameters on the observable dimensions, i.e.,

$$\zeta_{\xi_d,l} = \zeta_{\xi_d,l'}, \quad \forall d \leq \delta(L), \tag{92}$$

but differ on any unobserved dimension $d > \delta(L)$, then the corresponding columns in $\bar{\mathbf{A}}_1$ become identical:

$$\bar{\mathbf{A}}_1[:, l] = \bar{\mathbf{A}}_1[:, l']. \tag{93}$$

Therefore, the mapping from $(\zeta_{\theta_l}, \zeta_{\tau_l}, \zeta_{f_{\mathrm{D}}l})$ to $\bar{\mathbf{A}}_1[:, l]$ is non-injective, and naive selection of the first $L$ rows cannot in general guarantee $\mathrm{rank}(\bar{\mathbf{A}}_1) = L$ in the multidimensional Kronecker steering model.

## Appendix B
## Proof of Theorem 1

From (14), each column of $\bar{\mathbf{A}}$ is a Kronecker product of three Vandermonde vectors. Hence, for any index point $\boldsymbol{i} = (u_1, u_2, u_3) \in \mathcal{I}$ and target $l$, the corresponding entry of $\bar{\mathbf{A}}$ can be written as the monomial

$$\bar{\mathbf{A}}[\kappa(\boldsymbol{i}), l] = \zeta_{\theta_l}^{u_1-1} \zeta_{\tau_l}^{u_2-1} \zeta_{f_{\mathrm{D}}l}^{u_3-1}. \tag{94}$$

Therefore, $\bar{\mathbf{A}}_1 = \bar{\mathbf{A}}[\kappa(\mathcal{S}), :]$ is a generalized Vandermonde matrix whose entries are multivariate monomials with exponent vectors determined by $\mathcal{S}$.

Enumerate the selection of $L$ index points in $\mathcal{S}$ as $\{\boldsymbol{i}_s\}_{s=1}^{L}$ with $\boldsymbol{i}_s = (u_1(s), u_2(s), u_3(s))$, and define the corresponding exponent vectors

$$\boldsymbol{p}_s \triangleq [u_1(s) - 1,\ u_2(s) - 1,\ u_3(s) - 1]^\top \in \mathbb{Z}_{\geq 0}^3. \tag{95}$$

To show that $\det(\bar{\mathbf{A}}_1)$ is not identically zero, it suffices to exhibit one parameter realization for which $\bar{\mathbf{A}}_1$ is nonsingular. Let $\boldsymbol{a} = [a_1, a_2, a_3]^\top \in \mathbb{R}^3$ be an auxiliary projection vector and define

$$\begin{aligned} e_s &\triangleq \boldsymbol{a}^\top \boldsymbol{p}_s \\ &= a_1(u_1(s) - 1) + a_2(u_2(s) - 1) + a_3(u_3(s) - 1), \end{aligned} \tag{96}$$

We now show that, under the conditions (33)–(34), there exists a choice of $\boldsymbol{a}$ such that $\{e_s\}_{s=1}^{L}$ are pairwise distinct. Indeed, (33)–(34) imply that the set $\{\boldsymbol{p}_s\}$ is not contained in any affine subspace of dimension $\leq 2$ in $\mathbb{R}^3$; equivalently, there do not exist a nonzero $\boldsymbol{a}$ and a scalar $c$ such that $\boldsymbol{a}^\top \boldsymbol{p}_s = c$ holds for all $s$. Consequently, for any two distinct indices $s \neq s'$, we have $\boldsymbol{p}_s \neq \boldsymbol{p}_{s'}$, and the set of $\boldsymbol{a}$ satisfying $e_s = e_{s'}$ is the hyperplane

$$\mathcal{H}_{s,s'} \triangleq \left\{ \boldsymbol{a} \in \mathbb{R}^3 \,\middle|\, \boldsymbol{a}^\top (\boldsymbol{p}_s - \boldsymbol{p}_{s'}) = 0 \right\}, \tag{97}$$

which has Lebesgue measure zero. Since there are finitely many pairs $(s, s')$, the union $\cup_{s<s'} \mathcal{H}_{s,s'}$ also has measure zero, and thus there exists $\boldsymbol{a}$ outside this union such that $e_s \neq e_{s'}$ for all $s \neq s'$.

Now choose the target parameters as

$$\zeta_{\theta_l} = t^{a_1}, \quad \zeta_{\tau_l} = t^{a_2}, \quad \zeta_{f_{\mathrm{D}}l} = t^{a_3}, \quad l = 1, \ldots, L, \tag{98}$$

with an indeterminate $t > 0$. Substituting (98) into (94) yields

$$\bar{\mathbf{A}}_1[s, l] = t^{e_s}, \tag{99}$$

up to a nonzero column scaling (which does not affect singularity). Because the exponents $\{e_s\}$ are pairwise distinct, the matrix in (99) has a generalized Vandermonde structure with distinct exponents and is therefore nonsingular for all $t$ except a measure-zero set. Therefore, $\det(\bar{\mathbf{A}}_1)$ is a nonzero multivariate polynomial in $\{(\zeta_{\theta_l}, \zeta_{\tau_l}, \zeta_{f_{\mathrm{D}}l})\}_{l=1}^{L}$. Since a nonzero polynomial vanishes only on a measure-zero set, $\bar{\mathbf{A}}_1$ is nonsingular for generic target parameters.

## References


[1] T. Hwang, C. Yang, G. Wu, S. Li, and G. Y. Li, "OFDM and its wireless applications: A survey," *IEEE Transactions on Vehicular Technology*, vol. 58, no. 4, pp. 1673–1694, 2008.

[2] M. Bică and V. Koivunen, "Generalized multicarrier radar: Models and performance," *IEEE Transactions on Signal Processing*, vol. 64, no. 17, pp. 4389–4402, 2016.

[3] C.-X. Wang, X. You, X. Gao, X. Zhu, Z. Li, C. Zhang, H. Wang, Y. Huang, Y. Chen, H. Haas *et al.*, "On the road to 6G: Visions, requirements, key technologies and testbeds," *IEEE Communications Surveys & Tutorials*, 2023.

[4] J. A. Zhang, F. Liu, C. Masouros, R. W. Heath, Z. Feng, L. Zheng, and A. Petropulu, "An overview of signal processing techniques for joint communication and radar sensing," *IEEE Journal of Selected Topics in Signal Processing*, vol. 15, no. 6, pp. 1295–1315, 2021.

[5] A. Hassanien, M. G. Amin, E. Aboutanios, and B. Himed, "Dual-function radar communication systems: A solution to the spectrum congestion problem," *IEEE Signal Processing Magazine*, vol. 36, no. 5, pp. 115–126, 2019.

[6] L. Pucci, E. Paolini, and A. Giorgetti, "System-level analysis of joint sensing and communication based on 5G new radio," *IEEE Journal on Selected Areas in Communications*, vol. 40, no. 7, pp. 2043–2055, 2022.

[7] Z. Wei, Y. Wang, L. Ma, S. Yang, Z. Feng, C. Pan, Q. Zhang, Y. Wang, H. Wu, and P. Zhang, "5G PRS-based sensing: A sensing reference signal approach for joint sensing and communication system," *IEEE Transactions on Vehicular Technology*, vol. 72, no. 3, pp. 3250–3263, 2022.

[8] C. B. Barneto, T. Riihonen, M. Turunen, L. Anttila, M. Fleischer, K. Stadius, J. Ryynänen, and M. Valkama, "Full-duplex OFDM radar with LTE and 5G NR waveforms: Challenges, solutions, and measurements," *IEEE Transactions on Microwave Theory and Techniques*, vol. 67, no. 10, pp. 4042–4054, 2019.

[9] Y. Ge, F. Wen, H. Kim, M. Zhu, F. Jiang, S. Kim, L. Svensson, and H. Wymeersch, "5G SLAM using the clustering and assignment approach with diffuse multipath," *Sensors*, vol. 20, no. 16, p. 4656, 2020.

[10] Y. Ge, M. Stark, M. F. Keskin, F. Hofmann, T. Hansen, and H. Wymeersch, "V2X sidelink positioning in FR1: Scenarios, algorithms, and performance evaluation," *IEEE Journal on Selected Areas in Communications*, 2024.

[11] B. Friedlander, "On transmit beamforming for MIMO radar," *IEEE Transactions on Aerospace and Electronic Systems*, vol. 48, no. 4, pp. 3376–3388, 2012.

[12] Z. Xiao, R. Liu, M. Li, Q. Liu, and A. L. Swindlehurst, "A novel joint angle-range-velocity estimation method for mimo-ofdm isac systems," *IEEE Transactions on Signal Processing*, 2024.

[13] C. Sturm and W. Wiesbeck, "Waveform design and signal processing aspects for fusion of wireless communications and radar sensing," *Proceedings of the IEEE*, vol. 99, no. 7, pp. 1236–1259, 2011.

[14] K. M. Braun, "OFDM radar algorithms in mobile communication networks," Ph.D. dissertation, Karlsruhe, Karlsruher Institut für Technologie (KIT), Diss., 2014, 2014.

[15] S. Mercier, S. Bidon, D. Roque, and C. Enderli, "Comparison of correlation-based OFDM radar receivers," *IEEE Transactions on Aerospace and Electronic Systems*, vol. 56, no. 6, pp. 4796–4813, 2020.

[16] C.-Y. Chen and W.-R. Wu, "Joint AoD, AoA, and channel estimation for MIMO-OFDM systems," *IEEE Transactions on Vehicular Technology*, vol. 67, no. 7, pp. 5806–5820, 2018.

[17] Y. L. Sit, C. Sturm, J. Baier, and T. Zwick, "Direction of arrival estimation using the MUSIC algorithm for a MIMO OFDM radar," in *2012 IEEE radar conference*. IEEE, 2012, pp. 0226–0229.

[18] M. Wu and C. Hao, "Super-resolution TOA and AOA estimation for OFDM radar systems based on compressed sensing," *IEEE Transactions on Aerospace and Electronic Systems*, vol. 58, no. 6, pp. 5730–5740, 2022.

[19] C. R. Berger, B. Demissie, J. Heckenbach, P. Willett, and S. Zhou, "Signal processing for passive radar using OFDM waveforms," *IEEE Journal of Selected Topics in Signal Processing*, vol. 4, no. 1, pp. 226–238, 2010.

[20] J. B. Sanson, P. M. Tomé, D. Castanheira, A. Gameiro, and P. P. Monteiro, "High-resolution delay-Doppler estimation using received communication signals for OFDM radar-communication system," *IEEE Transactions on Vehicular Technology*, vol. 69, no. 11, pp. 13 112–13 123, 2020.

[21] Y. Liu, G. Liao, Y. Chen, J. Xu, and Y. Yin, "Super-resolution range and velocity estimations with OFDM integrated radar and communications waveform," *IEEE Transactions on Vehicular Technology*, vol. 69, no. 10, pp. 11 659–11 672, 2020.

[22] M. Mirabella, P. Di Viesti, A. Davoli, and G. M. Vitetta, "An approximate maximum likelihood method for the joint estimation of range and Doppler of multiple targets in OFDM-based radar systems," *IEEE Transactions on Communications*, 2023.

[23] L. Zheng and X. Wang, "Super-resolution delay-Doppler estimation for OFDM passive radar," *IEEE Transactions on Signal Processing*, vol. 65, no. 9, pp. 2197–2210, 2017.

[24] J. Sanson, A. Gameiro, D. Castanheira, and P. P. Monteiro, "Comparison of DoA algorithms for MIMO OFDM radar," in *2018 15th European radar conference (EuRAD)*. IEEE, 2018, pp. 226–229.

[25] X. Li and W. Yi, "A Subspace-Based Azimuth-Range-Doppler Estimator with Super-Resolution for OFDM Radar," in *2024 IEEE Radar Conference (RadarConf24)*. IEEE, 2024, pp. 1–6.

[26] Z. Hu, Q. Ye, Y. Huang, S. Hu, and G. Yang, "Joint Range-Velocity-Azimuth Estimation for OFDM-Based Integrated Sensing and Communication," *IEEE Transactions on Wireless Communications*, 2024.

[27] C. F. Caiafa and A. Cichocki, "Multidimensional compressed sensing and their applications," *Wiley Interdisciplinary Reviews: Data Mining and Knowledge Discovery*, vol. 3, no. 6, pp. 355–380, 2013.

[28] D. Nion and N. D. Sidiropoulos, "Tensor algebra and multidimensional harmonic retrieval in signal processing for MIMO radar," *IEEE Transactions on Signal Processing*, vol. 58, no. 11, pp. 5693–5705, 2010.

[29] H. Krim and M. Viberg, "Two decades of array signal processing research: the parametric approach," *IEEE Signal Processing Magazine*, vol. 13, no. 4, pp. 67–94, 1996.

[30] S. Marcos, A. Marsal, and M. Benidir, "The propagator method for source bearing estimation," *Signal processing*, vol. 42, no. 2, pp. 121–138, 1995.

[31] J. Sherman, "Properties of focused apertures in the Fresnel region," *IRE Transactions on Antennas and Propagation*, vol. 10, no. 4, pp. 399–408, 1962.

[32] R. Xie, D. Hu, K. Luo, and T. Jiang, "Performance analysis of joint range-velocity estimator with 2D-MUSIC in OFDM radar," *IEEE Transactions on Signal Processing*, vol. 69, pp. 4787–4800, 2021.

[33] S.-F. Chuang, W.-R. Wu, and Y.-T. Liu, "High-resolution AoA estimation for hybrid antenna arrays," *IEEE Transactions on Antennas and Propagation*, vol. 63, no. 7, pp. 2955–2968, 2015.

[34] Z. Yang, P. Stoica, and J. Tang, "Source resolvability of spatial-smoothing-based subspace methods: A hadamard product perspective," *IEEE Transactions on Signal Processing*, vol. 67, no. 10, pp. 2543–2553, 2019.

[35] S. U. Pillai and B. H. Kwon, "Forward/backward spatial smoothing techniques for coherent signal identification," *IEEE Transactions on Acoustics, Speech, and Signal Processing*, vol. 37, no. 1, pp. 8–15, 1989.

[36] R. Schmidt, "Multiple emitter location and signal parameter estimation," *IEEE transactions on antennas and propagation*, vol. 34, no. 3, pp. 276–280, 1986.

[37] J. Sanchez-Aranjo and S. Marcos, "Statistical analysis of the propagator method for DOA estimation without eigendecomposition," in *Proceedings of 8th Workshop on Statistical Signal and Array Processing*. IEEE, 1996, pp. 570–573.

[38] J. Xin, N. Zheng, and A. Sano, "Simple and efficient nonparametric method for estimating the number of signals without eigendecomposition," *IEEE Transactions on Signal Processing*, vol. 55, no. 4, pp. 1405–1420, 2007.

[39] J. Xin and A. Sano, "MSE-based regularization approach to direction estimation of coherent narrowband signals using linear prediction," *IEEE Transactions on Signal Processing*, vol. 49, no. 11, pp. 2481–2497, 2001.

[40] W. Liao, "MUSIC for multidimensional spectral estimation: Stability and super-resolution," *IEEE transactions on signal processing*, vol. 63, no. 23, pp. 6395–6406, 2015.

[41] R. Roy and T. Kailath, "ESPRIT-estimation of signal parameters via rotational invariance techniques," *IEEE Transactions on acoustics, speech, and signal processing*, vol. 37, no. 7, pp. 984–995, 1989.

[42] X. Zhang, L. Xu, L. Xu, and D. Xu, "Direction of departure (DOD) and direction of arrival (DOA) estimation in MIMO radar with reduced-dimension MUSIC," *IEEE Communications Letters*, vol. 14, no. 12, pp. 1161–1163, 2010.

[43] M. L. Rahman, J. A. Zhang, X. Huang, Y. J. Guo, and Z. Lu, "Joint communication and radar sensing in 5G mobile network by compressive sensing," *IET Communications*, vol. 14, no. 22, pp. 3977–3988, 2020.

[44] L. G. de Oliveira, B. Nuss, M. B. Alabd, A. Diewald, M. Pauli, and T. Zwick, "Joint radar-communication systems: Modulation schemes and system design," *IEEE Transactions on Microwave Theory and Techniques*, vol. 70, no. 3, pp. 1521–1551, 2021.

[45] A. Barabell, "Improving the resolution performance of eigenstructure-based direction-finding algorithms," in *ICASSP'83. IEEE International Conference on Acoustics, Speech, and Signal Processing*, vol. 8. IEEE, 1983, pp. 336–339.

[46] B. D. Rao and K. S. Hari, "Performance analysis of root-MUSIC," *IEEE Transactions on Acoustics, Speech, and Signal Processing*, vol. 37, no. 12, pp. 1939–1949, 1989.

[47] Y. Guercan and A. Yarovoy, "Super-resolution algorithm for joint range-azimuth-Doppler estimation in automotive radars," in *2017 European Radar Conference (EURAD)*. IEEE, 2017, pp. 73–76.

[48] R. Zhang, L. Cheng, S. Wang, Y. Lou, Y. Gao, W. Wu, and D. W. K. Ng, "Integrated sensing and communication with massive MIMO: A unified tensor approach for channel and target parameter estimation," *IEEE Transactions on Wireless Communications*, vol. 23, no. 8, pp. 8571–8587, 2024.

[49] P. Stoica and A. Nehorai, "MUSIC, maximum likelihood, and Cramer-Rao bound," *IEEE Transactions on Acoustics, speech, and signal processing*, vol. 37, no. 5, pp. 720–741, 1989.

[50] X. Zhang, H. Li, and B. Himed, "Multistatic detection for passive radar with direct-path interference," *IEEE Transactions on Aerospace and Electronic Systems*, vol. 53, no. 2, pp. 915–925, 2017.

[51] M. I. Skolnik *et al.*, *Introduction to radar systems*. McGraw-hill New York, 1980, vol. 3.